



— BUREAU OF —
RECLAMATION

**Desalination and Water Purification Research
and Development Program Report No. 225**

Thermoplasmonic Membrane Desalination

**U.S. Department of the Interior
Bureau of Reclamation
Technical Service Center
Denver, Colorado**

July 2021

REPORT DOCUMENTATION PAGE			Form Approved OMB No. 0704-0188		
The public reporting burden for this collection of information is estimated to average 1 hour per response, including the time for reviewing instructions, searching existing data sources, gathering and maintaining the data needed, and completing and reviewing the collection of information. Send comments regarding this burden estimate or any other aspect of this collection of information, including suggestions for reducing the burden, to Department of Defense, Washington Headquarters Services, Directorate for Information Operations and Reports (0704-0188), 1215 Jefferson Davis Highway, Suite 1204, Arlington, VA 22202-4302. Respondents should be aware that notwithstanding any other provision of law, no person shall be subject to any penalty for failing to comply with a collection of information if it does not display a currently valid OMB control number. PLEASE DO NOT RETURN YOUR FORM TO THE ABOVE ADDRESS.					
1. REPORT DATE (DD-MM-YYYY) 07-15-2021		2. REPORT TYPE Final		3. DATES COVERED (From - To) 3/1/2020-11/30/2020	
4. TITLE AND SUBTITLE Thermoplasmonic Membrane Desalination			5a. CONTRACT NUMBER Agreement No. R19AC0067		
			5b. GRANT NUMBER		
			5c. PROGRAM ELEMENT NUMBER		
6. AUTHOR(S) Todd Otanicar, Associate Professor Alejandro Espejo Sanchez, Graduate Research Assistant			5d. PROJECT NUMBER		
			5e. TASK NUMBER		
			5f. WORK UNIT NUMBER		
7. PERFORMING ORGANIZATION NAME(S) AND ADDRESS(ES) Boise State University, 1910 W University Dr., Boise, ID 83725			8. PERFORMING ORGANIZATION REPORT NUMBER		
9. SPONSORING/MONITORING AGENCY NAME(S) AND ADDRESS(ES) Bureau of Reclamation U.S. Department of the Interior Denver Federal Center PO Box 25007, Denver, CO 80225-0007			10. SPONSOR/MONITOR'S ACRONYM(S) Reclamation		
			11. SPONSOR/MONITOR'S REPORT NUMBER(S) DWPR Report No. 225		
12. DISTRIBUTION/AVAILABILITY STATEMENT Available from https://www.usbr.gov/research/dwpr/DWPR_Reports.html					
13. SUPPLEMENTARY NOTES					
14. ABSTRACT The potential for a hybrid desalination membrane and photovoltaic cell is proposed and tested experimentally and numerically. The membrane is doped with solar absorbing nanoparticles to both create thermal energy and reduce temperature polarization. The doped membrane exhibited a 15 to 32 percent increase in desalination performance (compared to an undoped membrane) when exposed to solar irradiance while simultaneously producing electrical power. The doped membranes in the hybrid configuration consistently produced over 20 L/m ² hr while producing an average of 0.36 W of power (at a module area of 225 cm ²) and solar irradiance values of ~600 W/m ² . While we have developed a heat and mass transfer model that can accurately replicate laboratory conditions with plain membranes, we are still completing work to validate the model for on-sun applications. One promising area is the potential for striped high efficiency but with opaque cells in the front of the membrane, as they will achieve much higher cell power output while resulting in similar light transmission to the membrane. Future work should focus on long-term testing, operation with higher levels of solar flux, and further development of an integrated system design.					
15. SUBJECT TERMS Solar, DCMD, membrane, nanoparticles					
16. SECURITY CLASSIFICATION OF:			17. LIMITATION OF ABSTRACT	18. NUMBER OF PAGES	19a. NAME OF RESPONSIBLE PERSON Saied Delegh
a. REPORT U	b. ABSTRACT U	THIS PAGE U			19b. TELEPHONE NUMBER (Include area code) (303) 445-2248

**Desalination and Water Purification Research
and Development Program Report No. 225**

Thermoplasmonic Membrane Desalination

**Prepared for the Bureau of Reclamation Under Agreement No.
R19AC00067**

by

Todd Otanicar Ph.D., P.E.

Alejandro Espejo Sanchez

Boise State University

**U.S. Department of the Interior
Bureau of Reclamation
Technical Service Center
Denver, Colorado**

July 2021

Mission Statements

The U.S. Department of the Interior protects and manages the Nation's natural resources and cultural heritage; provides scientific and other information about those resources; and honors its trust responsibilities or special commitments to American Indians, Alaska Natives, and affiliated Island Communities.

The mission of the Bureau of Reclamation is to manage, develop, and protect water and related resources in an environmentally and economically sound manner in the interest of the American public.

Acknowledgments

The Desalination and Water Purification Research and Development Program, Bureau of Reclamation, sponsored this research. Additional thanks go to Andrew Byrd, who served as an undergraduate student researcher and helped in membrane testing.

Acronyms and Abbreviations

Acronym or Abbreviation	Definition
AGMD	Air Gap Membrane Distillation
CA	Contact Angle
CB	Carbon Black
CFP	Capillary Flow Porometry
CNT	Carbon Nano-Tube
DCMD	Direct Contact Membrane Distillation
DI	Deionized
DIPS	Diffusion Induced Phase Separation
DLS	Dynamic Light Scattering
DMF	N,N-dimethylformamide
DRS	Diffuse Reflectance Spectra
DSC	Differential Scanning Calorimetry
DSSC	Dye Sensitized Solar Cell
ED	Electro Dialysis
EDS	Energy Dispersive X-ray Spectroscopy
FESEM	Field Emission Scanning Electron Microscopy
FF	Fill Factor
GHI	Global Horizontal Irradiance
IR	Infrared
LED	Light Emitting Diode
LEP	Liquid Entry Pressure
MD	Membrane Distillation
MED	Multi-Effect Distillation
MEMD	Multi-Effect Membrane Distillation
MF	Microfiltration
MGMD	Material Gap Membrane Distillation
MSF	Multi-Stage Flash
NESMD	Nanophotonic Enabled Solar Membrane Distillation
NF	Nanofiltration

Acronym or Abbreviation	Definition
NP	Nanoparticle
NWS	Non-Woven Support
PC	Polycarbonate
PP	Polypropylene
PS	Polysulfone
PS/ZnO	Polystyrene Zinc Oxide
PV	Photovoltaic
PVDF	Polyvinylidene Fluoride
RO	Reverse Osmosis
SEM	Scanning Electron Microscopy
SHC	Solar Heating and Cooling
TPC	Temperature Polarization Coefficient
UF	Ultrafiltration
UV	Ultraviolet
VMD	Vacuum Membrane Distillation

Measurements

Acronym or Abbreviation	Definition
%	percent transmittance/absorbance/reflectance/salt rejection
°C	degree Celsius
cm ²	square centimeters
L/m ² hr	liters per meters squared per hour
m ³	cubic meter
mA	milliamps
μm	micrometer
mm	millimeter
nm	nanometer
ppt	parts per thousand
rpm	revolutions per minute

Acronym or Abbreviation	Definition
V	volts
W	watts
W/m ²	watts per square meter

Variables

Acronym or Abbreviation	Definition
ρ	reflectance
λ	wavelength
η	efficiency
τ	transmittance
α	absorbance
E_{λ}	spectral solar irradiance
E_{solar}	solar irradiance
h	heat transfer coefficient
J_w	water flux across membrane
P_v	water vapor pressure
q	heat transfer rate
S	salinity
SR	salt rejection
T	temperature

This page intentionally left blank.

Table of Contents

Acronyms and Abbreviations	i
Measurements	ii
Variables	iii
Executive Summary	ix
1. Introduction	1
1.1. Project Background.....	1
1.1.1. Membrane Distillation Background.....	2
1.1.2. Solar Assisted MD Background.....	3
1.2. Project Overview	5
1.2.1. Overall Approach.....	6
1.2.2. Overall Method.....	7
2. Membrane Synthesis and Characterization	9
2.1. Materials.....	9
2.2. Membrane Synthesis	11
2.3. Optical Characterization.....	14
2.4. Morphological Characterization.....	16
3. Hybrid System Modeling	23
3.1. Heat and Mass transfer Model.....	23
3.2. Key Model Results.....	25
4. Hybrid PV + Membrane Distillation	27
4.1. DCMD Setup.....	27
4.2. PV Module Characterization.....	29
5. Results and Discussion	33
5.1. Desalination Results Off-Sun.....	33
5.2. Desalination Results On-Sun.....	37
6. Conclusions and Recommended Next Steps	43
6.1. Conclusions.....	43
6.2. Recommended Next Steps.....	44
7. Budget Spending	45
References	47

List of Figures

Figure 1. Detailed schematic representation of the temperature polarization phenomenon in MD..... 3

Figure 2. Schematic of hybrid photovoltaic-membrane desalination system, utilizing nanoparticle doped membrane..... 6

Figure 3. Commercial PVDF membrane: a) physical sample; b) spectral optical properties... 10

Figure 4. Schematic of custom phase inversion process..... 12

Figure 5. Membranes fabricated by custom phase inversion process: a) plain (Plain_0.0_Y_250), and b) doped (C-Cu_0.8_Y_250)..... 13

Figure 6. Spectral optical properties of the plain membrane fabricated via phase inversion. 15

Figure 7. Spectral optical properties of the doped membrane (0.8 percent by weight copper nanopowder carbon coated) fabricated via phase inversion..... 16

Figure 8. SEM images of the plain membrane fabricated via phase inversion: a) top surface; b) cross-section..... 18

Figure 9. SEM images of the doped membrane fabricated via phase inversion: a) top surface; b) cross-section..... 19

Figure 10. SEM images of a commercial PVDF membrane: a) top surface; b) cross-section... 20

Figure 11. Membrane contact angle images and measurements: a) plain membrane; b) doped membrane; c) commercial membrane..... 21

Figure 12. Transmittance of various solar cells..... 24

Figure 13. Water flux (a) and temperature (b) as a function of membrane position using perovskite cell..... 25

Figure 14. Water flux as a function of membrane length for different PV cells 26

Figure 15. Schematic diagram of proposed experiment (left) and setup during outdoor on-sun testing (right)..... 28

Figure 16. Semi-transparent solar modules: a) CdTe_30%_721; b) CdTe_40%_900; c) CdTe_60%_225; d) Silicon_30%_144..... 29

Figure 17. Spectral transmittance of two types of solar modules (CdTe_60%_225 and Silicon_30%_144) used in architectural glass applications..... 31

Figure 18. Plain membrane (Plain_0.0_Y_250) performance off-sun at standard conditions (permeate flux and salt rejection)..... 33

Figure 19. Doped membrane (C-Cu_0.8_Y_250) performance off-sun at standard conditions (permeate flux and salt rejection)..... 34

Figure 20. Plain (Plain_0.0_Y_250) and doped (C-Cu_0.8_Y_250) membrane performance off-sun at different feed temperatures (remaining experimental conditions maintained at standard conditions)..... 35

Figure 21. Plain (Plain_0.0_Y_250) and doped (C-Cu_0.8_Y_250) membrane performance off-sun at different feed flow rates (remaining experimental conditions maintained at standard conditions).....	36
Figure 22. Plain (Plain_0.0_Y_250) and doped (C-Cu_0.8_Y_250) membrane performance off-sun at different feed concentrations (remaining experimental conditions maintained at standard conditions).....	37
Figure 23. Photothermal effect on the plain membrane (Plain_0.0_Y_250) at standard conditions; comparison of off-sun to on-sun performances (GHI of 582 W/m ²).....	38
Figure 24. Summary of the photothermal effect on the plain membrane (Plain_0.0_Y_250) at standard conditions.....	38
Figure 25. Photothermal effect on the doped membrane (C-Cu_0.8_Y_250) at standard conditions; comparison of off-sun to on-sun performances (GHI of 617 and 698 W/m ²).....	39
Figure 26. Summary of the photothermal effect on the doped membrane (C-Cu_0.8_Y_250) at standard conditions.....	40
Figure 27. Summary of the photothermal effect on the plain membrane (Plain_0.0_Y_250) and the doped membrane (C-Cu_0.8_Y_250) at standard conditions.....	40
Figure 28. Solar module (CdTe_60%_225) effect on the photothermal effect of the doped membrane (C-Cu_0.8_Y_250) at standard conditions; membrane performance including and excluding the solar module (GHI of 508 and 698 W/m ² , respectively).....	41
Figure 29. Summary of the solar module (CdTe_60%_225) effect on the photothermal effect of the doped membrane (C-Cu_0.8_Y_250) at standard conditions.....	42
Figure 30. Desalination performance summary of the proposed hybrid PV-membrane system at standard conditions.....	44

List of Tables

Table 1. Summary of solar assisted membrane distillation work.....	5
Table 2. Summary of membrane fabrication parameters.....	13
Table 3. Summary of the membrane composition and weighted spectral absorptance at different carbon coated copper nanopowder weight percent ratios.....	15
Table 4. Comparison of solar properties and efficiency for each solar cell used in model.....	25
Table 5. Summary of CdTe thin film solar panels performance characterization.....	32
Table 6. Final budget for the award.....	45

This page intentionally left blank.

Executive Summary

The report details work conducted on the thermoplasmonic membrane desalination project since August 2019, when the team transferred to Boise State University. The project goal was to demonstrate the possible integration of solar photovoltaic (PV) module into a direct contact membrane distillation cell that is capable of directly absorbing thermal energy transmitted through the solar cell. The work was inevitably slowed down by the transfer of the team, negotiation, and the COVID-related shutdown of the laboratory that occurred from March to June.

The work focused on three primary efforts: completion of the experimental test setup, development of a successful membrane fabrication procedure, and validation of the numerical model. The membranes fabricated during this study exhibited a microporous, sponge-like, and hydrophobic nature during the morphological analysis. Scanning Electron Microscopy (SEM) images and contact angle measurements above 100° prove the suitability for membrane distillation (MD) applications. The membranes doped with a 0.8 weight percent load of carbon-coated copper nanoparticles increased the solar absorptance of the membrane by 80 percentage points during the optical analysis. A custom lab-scale direct contact membrane distillation setup characterizes the membranes fabricated off-sun and on-sun. The doped membrane exhibited a 15 to 32 percent increase in desalination performance (compared to an undoped membrane) when exposed to solar irradiance while simultaneously producing electrical power. The doped membranes in the hybrid configuration consistently produced over $20 \text{ L/m}^2\text{hr}$ while producing on average of 0.36 W of power (at a module area of 225 cm^2 and solar irradiance values of $\sim 600 \text{ W/m}^2$; these results are summarized in Figure ES-1.

While we have developed a heat and mass transfer model that can accurately replicate laboratory conditions with plain membranes, we are still completing work to validate the model for on-sun applications. One promising area is the potential for striped high efficiency, but opaque, cells in the front of the membrane, as they will achieve much higher cell power output while resulting in similar light transmission to the membrane. Future work should focus on long-term testing, operation with higher levels of solar flux, and further development of an integrated system design.

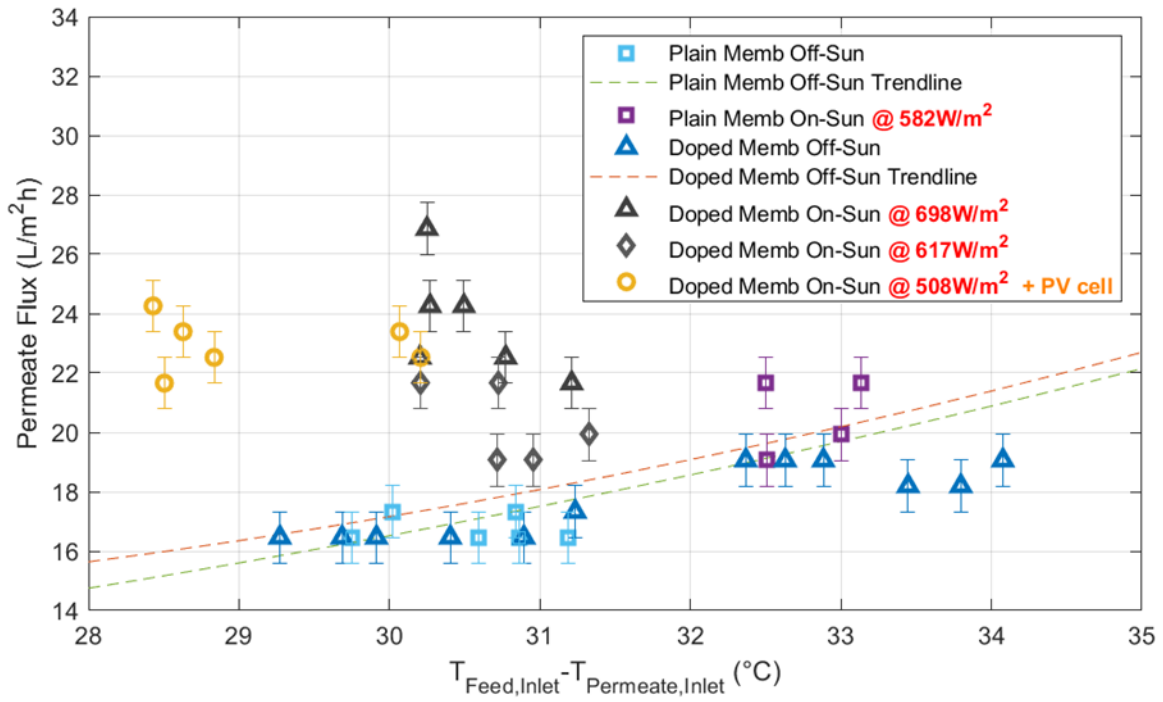


Figure ES-1. Desalination performance summary of the proposed hybrid PV-membrane system at standard conditions

1. Introduction

In this project, a novel hybrid membrane distillation plus photovoltaic (PV) cell was developed that is capable of co-producing electricity and clean distillate. At the core of the technology is a membrane doped with solar-absorbing nanoparticles (NPs) that only absorb wavelengths not transmitted through a PV cell. This provides the means to integrate the system but also provides an avenue for increasing the temperature polarization coefficient and improving membrane performance. The membranes were fabricated using phase inversion and knife casting for ease of fabrication and incorporation of NPs. The project culminated with the development of a 25 cm² prototype for on-sun demonstration of the hybrid approach.

The funds used for this project supported the synthesis of the NPs, fabrication and characterization of the membranes, development of the coupled heat and mass transfer and electrical model, and overall system design/build/testing. The project focused on improved membrane system performance through controlled temperature polarization, and on novel approaches to desalinate water that reduce primary energy use through the use of a hybrid design where heat is provided from PV cell waste heat.

Overall, the project could lead to increased use of renewable energy for desalination while improving the ability to use membrane distillation (MD) for desalination purposes. This could be especially useful in places with limited access to grid-scale electric and/or thermal power, as this hybrid system could be deployed to not only produce electricity but also co-produce clean water. One potentially attractive area for this type of system is in the treatment and disposal of produced water from oil and natural gas operations. In many of these operations, grid access is extremely limited and on-site electricity is being produced with generators to not only power wellhead equipment but also to power water treatment and disposal methods.

1.1. Project Background

Distillation is one type of water treatment process that involves the complete separation of vapor molecules from a liquid mixture via boiling, transportation of the vapor to a cooler location, saturation of the water vapor, and condensation into clean water (Drioli et al. 2015). Furthermore, MD is a thermally-driven process in which a microporous hydrophobic membrane acts as the physical barrier between the feed solution and the permeate solution. This thermal process only allows the separation of vapor molecules from the feed solution to pass through the membrane pores and condense on the permeate side. As the process is non-isothermal, the temperature difference existing between both solutions creates a temperature gradient through the liquid and vapor interfaces. This temperature gradient is responsible for the vapor pressure difference between the membrane surfaces, which is, ultimately, the driving force of the process (Al-Obaidani et al. 2008; Alkhudhiri et al. 2012).

1.1.1. Membrane Distillation Background

MD has considerable advantages over the conventional distillation processes of reverse osmosis (RO), multi-effect distillation (MED), or multi-stage flash (MSF). The feed solution is not required to boil, so lower operating temperatures are required. Therefore, the hydrostatic pressure required is lower and the process equipment is much smaller, making MD a more cost-effective process (Mahdi et al. 2015). The reduced chemical interaction between the membrane and the feed solution requires less demanding membrane mechanical characteristics, and less expensive materials can be used in the manufacturing process. The membrane pore size required is relatively larger than other separation processes, such as RO, so less fouling occurs.

Theoretically, MD is a complete separation process due to the vapor-liquid equilibrium, so a higher rejection factor is achieved (Alkhudhiri et al. 2012). Performance is not limited by the osmotic pressure or the concentration polarization, and higher salinity levels can be reached (Al-Obaidani et al. 2008). Moreover, MD systems have the flexibility to be combined with other separation processes, such as ultrafiltration (UF), nanofiltration (NF), or RO, for highly purified permeates and are attractive to pair with low grade heat and renewable energy sources such as solar, wind, or geothermal for more ecological and cost-effective systems (Qtaishat and Banat 2013).

Although MD has many advantages, it also has some drawbacks that must be solved for optimum performance. These obstacles are membrane pore wetting, high conductive heat loss, and the temperature polarization phenomenon (Abu-Zeid et al. 2015). The main factors affecting membrane wetting are the surface tension of the feed solution, the membrane material, and the membrane structure (Qtaishat and Banat 2013). These factors can be improved by using a membrane with a high water liquid entry pressure (LEP), which is achieved by using a membrane with high hydrophobicity and a small maximum pore size. Conductive heat loss can be reduced by utilizing a thick and highly porous membrane. The conductive heat transfer coefficient of the gas trapped inside the membrane is an order of magnitude smaller than the coefficient of the solid membrane material, so the porosity of the membrane is particularly important (AlMarzooqi et al. 2016). The temperature polarization phenomenon consists of the gradual decrease of temperature at the thermal boundary layers of the membrane due to the large amount of heat consumed and released in the process of phase transition, reducing the supply of heat for evaporation to the feed-membrane interface (Cath et al. 2004; Chernyshov et al. 2005). It is defined as the difference between the theoretical driving force and the actual driving force. The theoretical driving force is determined as the difference between the bulk feed temperature (T_{bf}) and the bulk permeate temperature (T_{bp}), while the actual driving force is determined as the temperature difference between the feed-membrane interface temperature (T_{mf}) and the permeate-membrane interface temperature (T_{mp}) (Manawi et al. 2014). Figure 1 is a simple schematic of the temperature polarization phenomenon.

The heat losses in MD can negatively affect the process by reducing the driving force by up to 80 percent (Manawi et al. 2014), leading to a drop in the flux across the membrane. The mathematical expression of this phenomenon is the temperature polarization coefficient (TPC), which is defined as the ratio between the actual driving force and the theoretical driving force and should be as close as possible to unity.

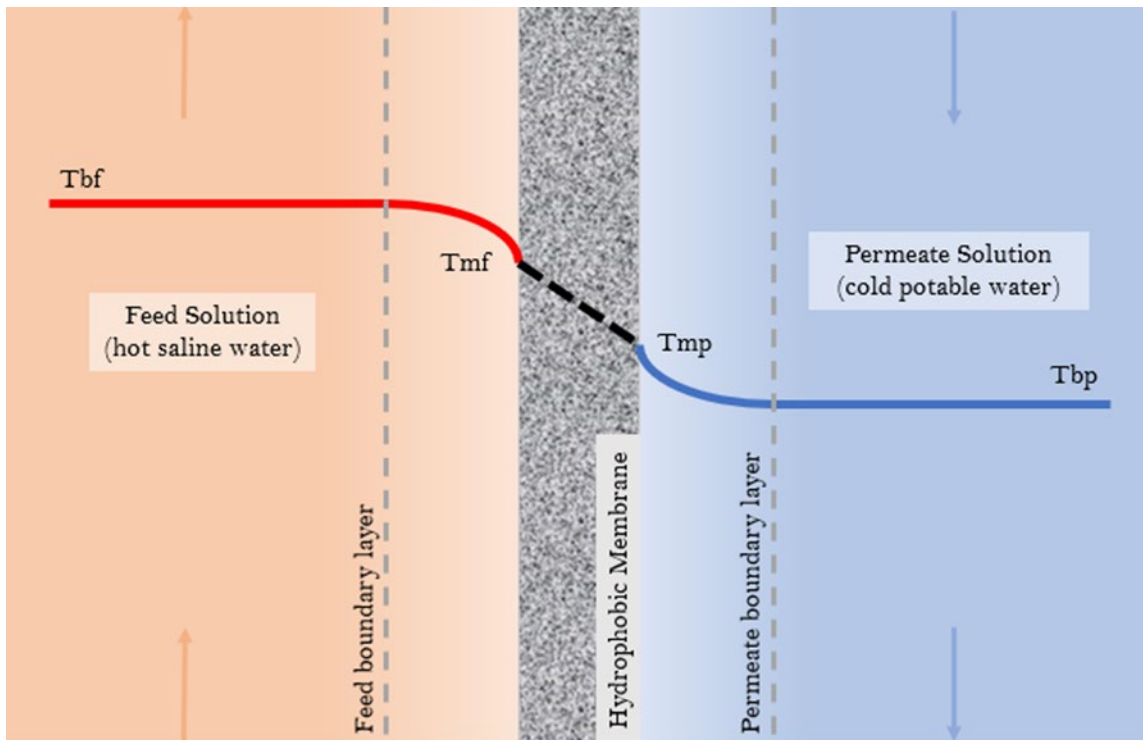


Figure 1. Detailed schematic representation of the temperature polarization phenomenon in MD

MD is mainly used for the distillation of brackish waters and seawaters at an affordable cost of \$1.32 per m^3 (Al-Obaidani et al. 2008). Moreover, it can be used as a supplement or as an alternative to the conventional distillation processes. However, the application field for this process is wide, and water recovery from wastewater streams is one of the most promising applications for the future.

Furthermore, other applications where MD has been used are: treatment of radioactive waste where the product could be safely discharged to the environment; treatment of concentrated fruit juices and sugar solutions in the food industry; sterilization of biological fluids at high temperatures for the medical industry; removal of organic and heavy metals from aqueous solutions in the environmental industry; treatment of produced water after fracking containing very high levels of salts, various hydrocarbons, and production chemicals in the oil and gas industry; and temperature-sensitive products such as pharmaceutical compounds, dairy products, natural aromatic compounds, and solutions of several chemicals.

1.1.2. Solar Assisted MD Background

Solar assisted MD has been broadly examined to deliver the thermal and electrical energy required to run the desalination process. Using solar PV cells to provide the electrical power and solar collectors to provide the thermal energy are configurations commonly used in solar technologies coupled with membrane distillation (Qtaishat and Banat 2013). The cost associated with these technologies can range from \$8.9 per m^3 to \$18 per m^3 , where the membrane and plant lifetime are the key parameters. An example of solar assisted MD is the MEDESOL project, which assesses a cost-effective and high-efficiency multistage membrane distillation

concept. The solar multistage MD system involves the integration of multiple membrane distillation modules coupled to a solar concentrator for thermal energy (Blanco et al. 2009). More solar assisted MD projects are summarized by Mahdi et al. in their membrane distillation review (Mahdi et al. 2015). During this review, a total of six systems coupled with thermal or electrical energy sources are organized chronologically.

It is, however, difficult to find an analysis of a potential combination of PV or thermal with desalination in a hybrid system or directly heating the membrane with solar energy. Calise et al. presented novel work by developing a polygeneration system consisting of a concentrating PV/thermal collector, solar heating and cooling (SHC), and MED (Calise et al. 2014). Their numerical case study reveals the potential energy saving this type of system provides. Summers et al. patented an air gap membrane distillation (AGMD) system, which includes a dyed solar absorbing membrane positioned to receive solar radiation as the thermal input (Summers and Lienhard V 2013)]. Dongare et al. demonstrated photothermal heating induced by solar irradiance in a nanophotonic enabled solar membrane distillation (NESMD) configuration (Dongare et al. 2017). An optical absorbing coating layer on top of the membrane was capable of producing enough localized photothermal heating to drive the distillation process and thus eliminate the requirement of heating the input water.

An innovative approach to influence the temperature polarization was introduced by Vanherck et al. via plasmonic heating (Vanherck et al. 2011)]. They demonstrated an increase of flux by incorporating gold NPs into the membrane and irradiating the membrane with laser light close to the surface plasmon resonance wavelength of the NPs. The NPs experience plasmonic heating when they are exposed to wavelengths of light corresponding to the plasmon resonance; thus, they are capable of converting light into heat energy efficiently. To guarantee a high light-to-heat conversion efficiency, NPs with significant absorption efficiencies and poor luminescence quantum yields are necessary (Politano et al. 2016). Further work with gold NPs and laser irradiance illustrates the concept of localized thermal heating (Li et al. 2013).

The study of photothermal heating has been extended to other type of NPs and light sources. Li et al. replaced gold NPs and laser radiation with silver NPs and light emitting diode (LED) light. They proved that this combination is a good alternative to the previous study regarding performance and cost (Li et al. 2014). In further studies, they demonstrated the potential of plasmonic heating by irradiating ultraviolet (UV) light to membranes incorporating silver NPs. They demonstrated an increase in flux and bulk membrane temperatures with increased NP loading (Politano et al. 2019).

More recently, carbon black NPs have been employed for plasmonic heating. Dongare et al. coated a layer of carbon black NPs over an existing membrane and induced highly localized photothermal heating by solar illumination to drive the distillation process (Dongare et al. 2017). Similarly, Lind exposed a coated membrane to simulated solar irradiance to enhance the desalination permeate flux (Lind 2018).

The tunability of plasmonics has recently emerged as a new route to enhance the photothermal effect by the colloidal synthesis of nanostructures. Dopant distribution presents a new frontier of opportunity for tunable plasmonic materials (Lounis et al. 2014). Extensive work has been

done to prove the concept of photothermal heating and its possible enhancement. Pioneer work regarding nanoshells was done by Oldenburg et al. after they revealed that the optical resonance of a metal nanoshell, a dielectric core, and a metallic shell can be modified in a controlled fashion. By varying the core and shell dimensions, they demonstrated the wavelength optical resonance shift over hundreds of nanometers (Oldenburg et al. 1998).

The addition of NPs is also demonstrated to have an impact on membrane performance (Roshani et al. 2018). Roshani et al. showed evidence that the addition of polystyrene/zinc oxide (PS/ZnO) caused an increase in porosity, surface roughness, and contact angle, which ultimately resulted in a significant increase in membrane performance. Similarly, Tijing et al. fabricated superhydrophobic membranes by coating a layer of carbon nanotubes on top of a nanofiber membrane to enhance the hydrophobicity of the membrane, and, therefore, the permeate flux (Tijing et al. 2016).

Table 1 presents a summary of solar assisted membrane distillation work.

Table 1. Summary of solar assisted membrane distillation work

Article Author	MD Configuration	Light Source	NP Type	PV system	Water Flux (L/m ² h)	Light Flux (W/m ²)
Dongare et al.	NESMD	Sunlight	Carbon Black (CB)	None	1.12	0
					2.72	700
Vanherck et al.	Dead-end filtration	Laser	Gold	None	1.5	0
					1.75	2000
Li et al. (2013)	Dead-end filtration	Argon laser	Gold	None	0.7	0
					0.9	5000
Li et al. (2014)	Dead-end filtration	LED	Silver	None	1.1	0
					1.2	0.21
Politano et al. (2019)	VMD	UV lamp	Silver	None	3	0
					25.7	2.3e10 ⁴
Lind	Pervaporation	Xenon lamp	Carbon Black (CB)	None	1.2	0
					1.9	23000

1.2. Project Overview

The opportunity identified in the previous sections resulted in this new study to provide awareness of a system capable of supplying electrical energy and clean distillate while

overcoming distillation drawbacks such as temperature polarization and conduction heat losses. A direct contact membrane distillation (DCMD) configuration was selected from all MD configurations, as well as a PV, due to the simplicity of building the system for research purposes.

1.2.1. Overall Approach

The proposed design considers the advantages of MD by combining DCMD with a PV cell. This hybrid design consists of a membrane distillation system with a PV cell incorporated on top of the direct contact membrane module. As the first layer of the design, the PV cell collects a portion of the visible solar spectrum while allowing the remaining energy to pass through and reach the membrane module. Next, the filtered solar energy travels through a second layer, the feed stream, helping to warm the stream and lower the system energy requirements. The energy then reaches the membrane, a third and final layer of the design, at the core of the module, where it can be absorbed, reflected, or transmitted. In order to absorb most of the energy reaching the membrane, NPs of different chemical compositions can be doped into the membrane. This process helps to mitigate the temperature polarization effect and the conduction losses, which are principal disadvantages of DCMD, and therefore helps to improve the permeate flux of the system. Figure 2 shows a schematic of the proposed design.

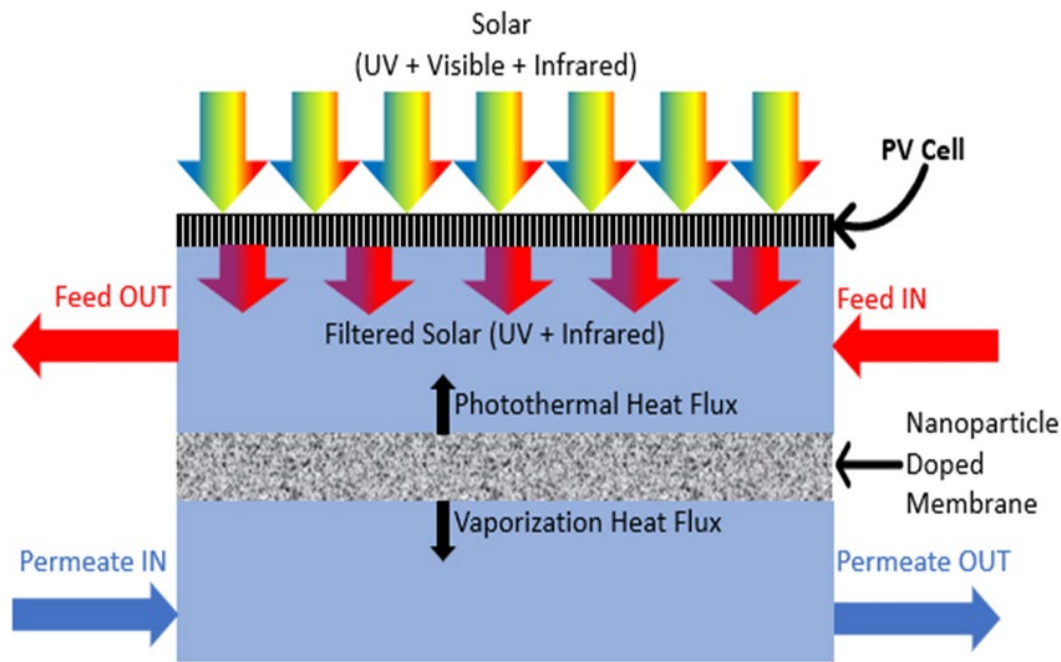


Figure 2. Schematic of hybrid photovoltaic-membrane desalination system, utilizing nanoparticle doped membrane

This hybrid design has been previously simulated to prove its potential. Kinzer et al. developed a theoretical model to investigate the role of the solar concentration level, and the lower wavelength of the spectral filtration, on both the water flux and the electrical production from the PV cell (Kinzer et al. 2018). The work completed for this project focuses on the

development of an experimental test bed capable of demonstrating the proposed concept and validating the model.

1.2.2. Overall Method

This study was designed to address three high-level objectives: the synthesis and characterization of selectively absorbing NP doped membranes (presented in Section 2); the design and characterization of a hybrid membrane distillations and photovoltaic cell system (presented in Section 3); and the development of a heat and mass transfer model (presented in Section 4).

Section 2 focuses on developing a membrane synthesis process capable of incorporating NPs and the characterization of the membranes fabricated. The synthesis process must result in a microporous hydrophobic membrane with a uniform distribution of NPs across the membrane volume and with a contact angle equal to or higher than 90 degrees (AlMarzooqi et al. 2016). Moreover, the NPs doped into the membrane must be capable of enhancing the energy absorption for wavelengths across the whole solar spectrum.

Section 3 focuses on the design, construction, and performance characterization of a hybrid MD with a PV cell prototype incorporating the proposed membrane module. The experimental system must include two closed loops, the feed and the permeate streams, capable of providing the necessary testing conditions on each side, and a data acquisition system for data logging. Moreover, the characterization off-sun and on-sun of the hybrid system is required. The system must be able to co-produce electrical energy and clean distillate while mapping the system performance at different testing conditions. Specifically, the system with an NP doped membrane must be able to distill water at a higher rate than the system using an undoped membrane, proving the enhancement of the temperature polarization effect and the permeate flux due to the NP localized photothermal heating. In order to verify the effect of the hybrid design, including NPs in the membrane and a PV cell on top of the membrane module, a set of tests is required that includes tests run indoors and outdoors for direct comparison. Experimental testing covers multiple feed and permeate temperatures, feed and permeate flow rates, and feed salinity levels.

Section 4 details the heat and mass transfer model development. While the model has been used to verify previous results, ongoing work is still focused on verifying model predictions with the experimental results obtained in this study.

This page intentionally left blank.

2. Membrane Synthesis and Characterization

This chapter focuses on the first high-level objective of the study, the development of a membrane synthesis process capable of incorporating NPs and the optical and morphological characterization of the fabricated membranes.

2.1. Materials

Hydrophobic polymers are commonly selected for the synthesis of MD membranes due to their characteristics of easy fabrication, modification, scale-up, and low cost (Wang and Chung 2015). Polyvinylidene fluoride (PVDF) is selected in this case as the base polymer for the membrane synthesis due to its easy processability, thermal stability, hydrophobicity, mechanical strength, and resistance to corrosive chemicals characteristics (Feng et al. 2013; Lalia et al. 2013). This semi-crystalline polymer contains a crystalline phase, which provides thermal stability, and an amorphous phase, which provides flexibility towards membrane applications (Wang and Chung 2015). Moreover, the affinity between the solvent and the polymer is the most influential parameter in the membrane permeate flux (Dobrak-Van Berlo et al. 2011). N,N-dimethylformamide (DMF) is selected in this case as the base solvent for an easy dissolution with the base polymer and quick precipitation during the immersion process.

Materials used in traditional membranes do not exhibit high solar absorption; see Figure 3. However, NPs are an attractive solution for modifying the optical properties of the membrane due to their high absorption characteristics at low particle loadings. Noble metal NPs are specifically excellent absorbers of visible light due to their surface plasmon resonance characteristics (Jain et al. 2006). Although any NP can enhance the absorption of a membrane, NPs with high absorption characteristics such as carbon nanotubes or graphite are desirable for this application (Goel et al. 2020).

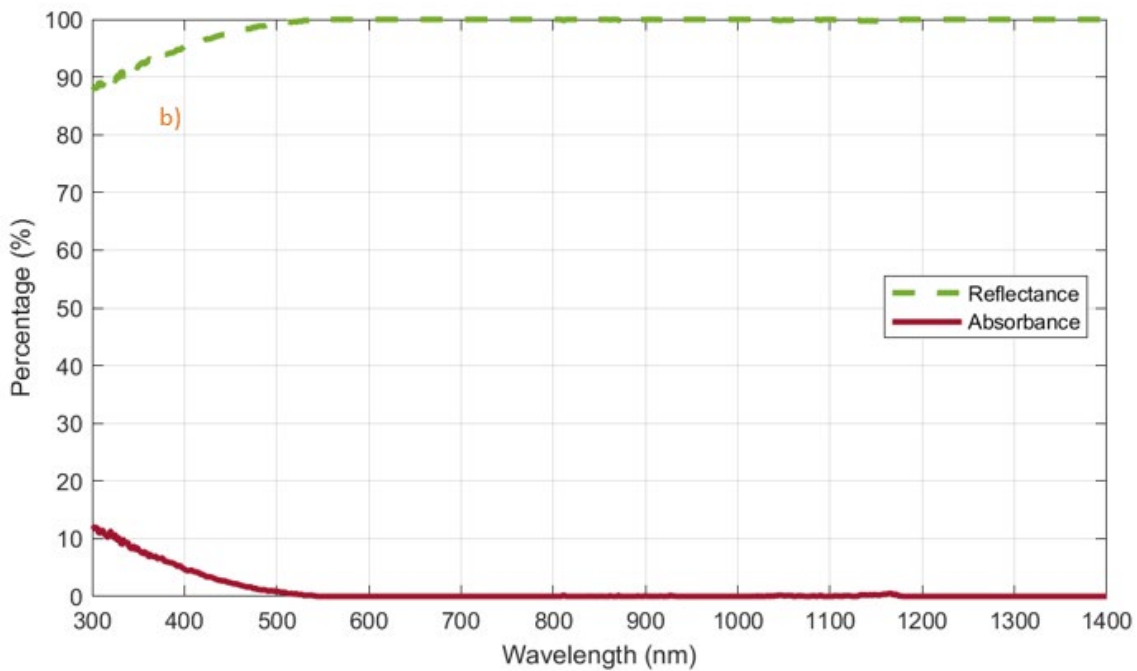


Figure 3. Commercial PVDF membrane: a) physical sample; b) spectral optical properties

The base solution for the membranes used in this study is made out of PVDF (HSV900, >99% by weight, kindly provided by Arkema) as the polymer, and DMF (DX1730, Sigma Aldrich) as the solvent. The NPs considered for doping purposes of the base solution are carbon coated copper nanopowder (Cu, carbon coated, 99.8%, 25 nm, Nanoamor), silver nanopowder (Ag, 99.95%, 100nm, SkySpring Nanomaterials, Inc.), and gold coated silica nanoshells (Au SiO₂, 85nm, nanoComposix). The hydrophobic membranes fabricated with only the base solution are considered plain PVDF membranes, while the membranes containing NPs are considered doped membranes. The nomenclature for plain and doped membranes fabricated during this study is

the following: “NP type_NP weight percent (wt%)_Addition of support (Y/N)_Casting membrane thickness (μm).”

2.2. Membrane Synthesis

Phase inversion is a commonly used technique for the fabrication of membranes in previous work. The process can be used for the fabrication of plain membranes as in the Khayet and Matsuura study (Khayet and Matsuura 2001), or it can be altered by adding additives or NPs to investigate the effect on morphology and transport properties. An important factor during the phase inversion process for non-supported membranes is shrinkage. Although there is little information in the literature, Bilad et al. addressed the relevance of this phenomenon (Bilad et al. 2015). The polymer is subjected to an action force after a film is casted, which draws the polymer towards the center of the film and causes shrinkage. This force is due to a difference in surface tension between the film casted and the air before the coagulation bath, and between the film and the water during the bath. This phenomenon is commonly solved using non-woven supports (NWS), which provide enough mechanical strength to overcome the shrinkage force. The study also reported a shrinkage increase as the casting thickness and the polymer concentration increases.

In this study, a custom phase inversion process fabricates the synthesized plain membranes. An immersion precipitation is specifically selected for a diffusion induced phase separation (DIPS) process due to the simplicity of the process for research purposes. First, 89 percent by weight of solvent (DMF) is added into a jar and placed on a magnetic stirrer (MR HEI-standard Heidolph). Then, 11 percent by weight of polymer (PVDF) is added gradually to the jar to mix the components at ambient temperature and 150 revolutions per minute (rpm) for 24 hours. The mixed solution is placed in a standard chamber connected to a vacuum pump (DV-4E-250 eliminator) for de-gas during at least 2 hours or until all bubbles are released. Next, the solution is casted over a non-woven support (Novatexx 2483, kindly provided by Freudenberg) by using an adjustable doctor blade with an automatic film coater (MTI corporation MSK-AFA-II) at a speed of 10 mm/second and a casting thickness of 250 μm . The membrane is quickly immersed into a non-solvent coagulation bath containing deionized (DI) water at room temperature for immersion precipitation and maintained for 24 hours to remove any solvent residue. Finally, the membrane is dried in an oven at 60°C for 24 hours to evaporate all traces of solvent and complete cross-linking; see Figure 4 for a graphical description.

The doped membranes synthesized in this study result from the combination of ultrasonication and the phase inversion process above. Ultrasonication is necessary as a pre-step for the adequate dispersion of the NPs in the solvent. First, 89 percent by weight of solvent and 0.8 percent by weight of NPs (25 nm of Cu carbon coated) are added into a jar and placed inside a chamber for ultrasonication (Q500 sonicator) during 15 minutes at 50/10 second intervals and 30 percent amplitude. Following ultrasonication, the mixture is placed on a magnetic stirrer, where 10.2 percent by weight of polymer is added gradually. The subsequent steps replicate the phase inversion process used for the synthesis of plain membranes.

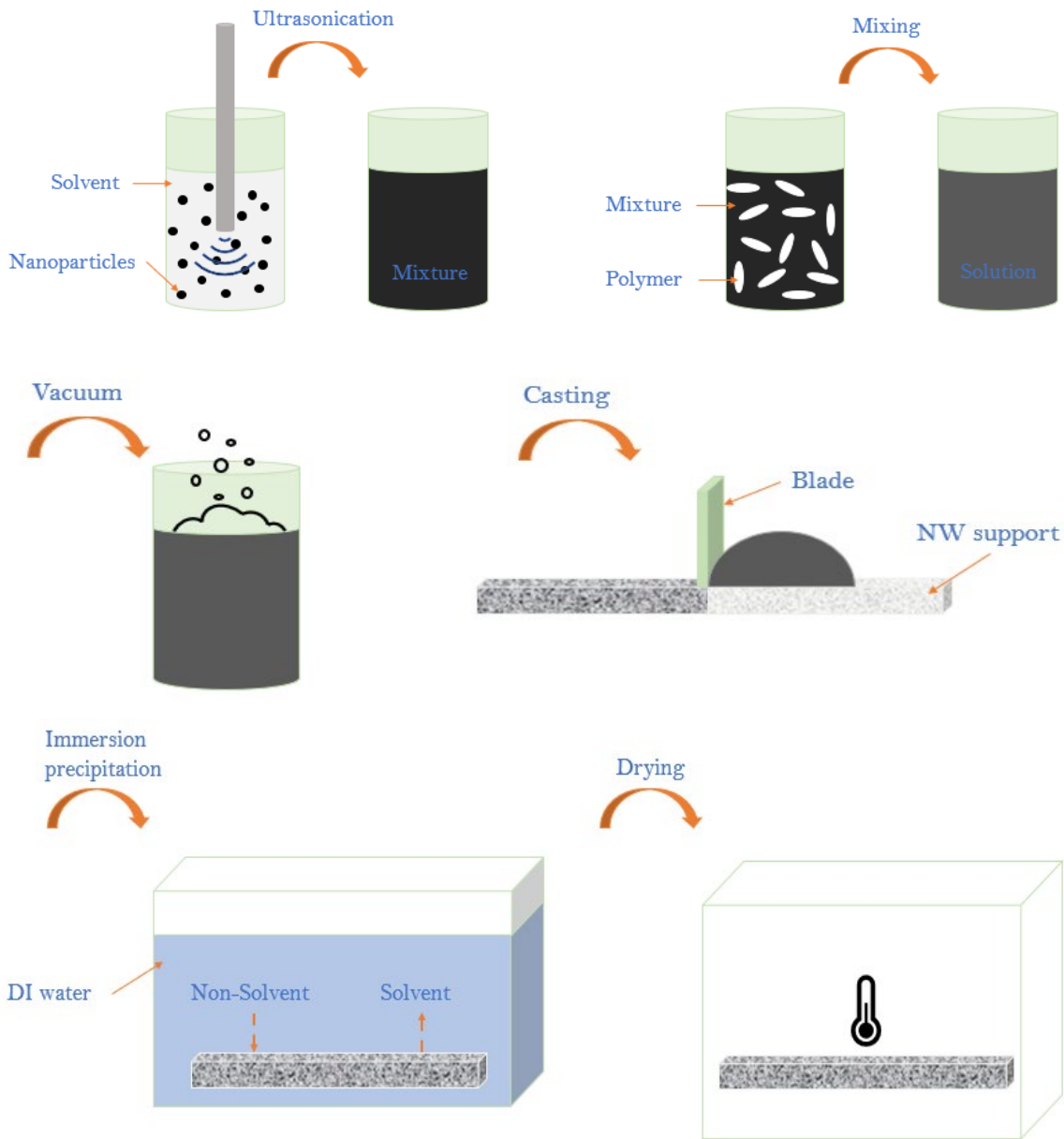


Figure 4. Schematic of custom phase inversion process

Figure 5 displays the final membranes, plain and doped, produced by the developed phase inversion process and used for performance characterization. Table 2 summarizes the composition of the different membranes fabricated during this study. The plain and doped membranes are employed to accomplish the project’s objectives, while the remaining membranes are trials used in a preliminary analysis to determine the best possible NP doping option.



Figure 5. Membranes fabricated by custom phase inversion process: a) plain (Plain_0.0_Y_250), and b) doped (C-Cu_0.8_Y_250)

Table 2. Summary of membrane fabrication parameters

Membrane Name	NWS Type	Casting Thickness (μm)	PVDF (wt%)	DMF (wt%)	NP Type	NP (wt%)
<i>Plain_0.0_Y_250</i> ("Plain Membrane")	Novatexx 2483	250	11.0	89.0	None	0.0
<i>C-Cu_0.8_Y_250</i> ("Doped Membrane")	Novatexx 2483	250	10.2	89.0	C-Cu	0.8
<i>Plain_0.0_N_120</i>	None	120	16.0	84.0	None	0.0
<i>Au-SiO₂_0.8_N_120</i>	None	120	15.6	83.6	Au-SiO ₂	0.8
<i>Ag_0.8_N_120</i>	None	120	15.6	83.6	Ag	0.8
<i>C-Cu_0.8_N_120</i>	None	120	15.6	83.6	C-Cu	0.8

2.3. Optical Characterization

The membranes fabricated during this study are characterized by analyzing their spectral characteristics. A spectrophotometer (Shimadzu UV-2600) measures the reflectance and transmittance across a wavelength range of 300 to 1400 nm. In this case, the light spectrum determines the energy the membrane receives after filtration by the PV cell. The solar weighted spectral reflectance (ρ) and transmittance (τ) of the membrane are calculated according to Equations (2.1) and (2.2). Moreover, the solar weighted spectral absorptance (α) is calculated according to Equation (2.3) (Duffie and Beckman 2013):

$$\rho = \frac{\int_0^{\infty} \rho_{\lambda} E_{\lambda} d\lambda}{\int_0^{\infty} E_{\lambda} d\lambda} \quad (2.1)$$

$$\tau = \frac{\int_0^{\infty} \tau_{\lambda} E_{\lambda} d\lambda}{\int_0^{\infty} E_{\lambda} d\lambda} \quad (2.2)$$

$$\alpha = 1 - \tau - \rho \quad (2.3)$$

Where ρ_{λ} is the spectral reflectance, τ_{λ} is the spectral transmittance, and E_{λ} is the spectral emissive power obtained from ASTM – G173.

A preliminary analysis of the trial membranes doped with different NPs, specified in Table 2, was conducted to identify the best possible option for doping purposes. The analysis also determined the amount of NPs added during the synthesis process. The type of NP and the weight percent ratio presenting the highest absorptance from this analysis were selected to pursue the project's objectives. Subsequently, the final plain and doped membranes were characterized in the same manner.

According to the preliminary analysis of the NPs' optical properties, the copper nanopowder coated with black carbon presents the best absorptance. Table 3 proves this statement by showing the results of all three NPs considered. Based on this result, the carbon coated copper nanopowder is adopted for doping purposes. Additionally, the notch in the absorptance performance observed at the transition from the visible to the infrared spectrum is attributed to noise in the system.

Moreover, the data in Table 3 prove that the addition of 0.8 percent by weight NP at a thickness greater or equal to 240 μm provides a solar weighted spectral absorptance above 90 percent. This substantial increase of absorptance, in addition to the small variation of the membrane chemical composition, leads to the selection of 0.8 percent by weight NP as the doping concentration of the final doped membrane. The preliminary analysis results lead to the selection of the membranes "Plain_0.0_Y_250" and "C-Cu_0.8_Y_250" for the completion of this project's objectives. Furthermore, the membranes "Plain_0.0_Y_250" and "C-Cu_0.8_Y_250" will be referred to as "Plain Membrane" and "Doped Membrane," respectively, throughout the remainder of this document.

Table 3. Summary of the membrane composition and weighted spectral absorptance at different carbon coated copper nanopowder weight percent ratios

Membrane Name	NWS Type	Casting Thickness (μm)	PVDF (wt%)	DMF (wt%)	NP Type	NP (wt%)	Absorptance (%)
<i>C-Cu_0.1_N_120</i>	None	120	15.6	83.6	C-Cu	0.1	40.3
<i>C-Cu_0.1_N_240</i>	None	240	15.6	83.6	C-Cu	0.1	63.2
<i>C-Cu_0.8_N_120</i>	None	120	15.6	83.6	C-Cu	0.8	69.0
<i>C-Cu_0.8_N_240</i>	None	240	15.6	83.6	C-Cu	0.8	92.3
<i>C-Cu_0.8_Y_250</i>	Novatexx 2483	250	10.2	89.0	C-Cu	0.8	83.1
<i>C-Cu_2.4_Y_250</i>	Novatexx 2483	250	9.4	88.2	C-Cu	2.4	91.4

The plain membrane (Plain_0.0_Y_250) used during this study exhibits a high reflectance and a near zero absorptance across the selected wavelength range, which results in a lower permeate flux due to the temperature polarization effect and a higher thermal input required for the feed stream when exposed to solar irradiance. Specifically, the weighted spectral reflectance and absorptance are 96.4 percent and 3.5 percent, respectively. Figure 6 exhibits the optical characterization of the plain membrane.

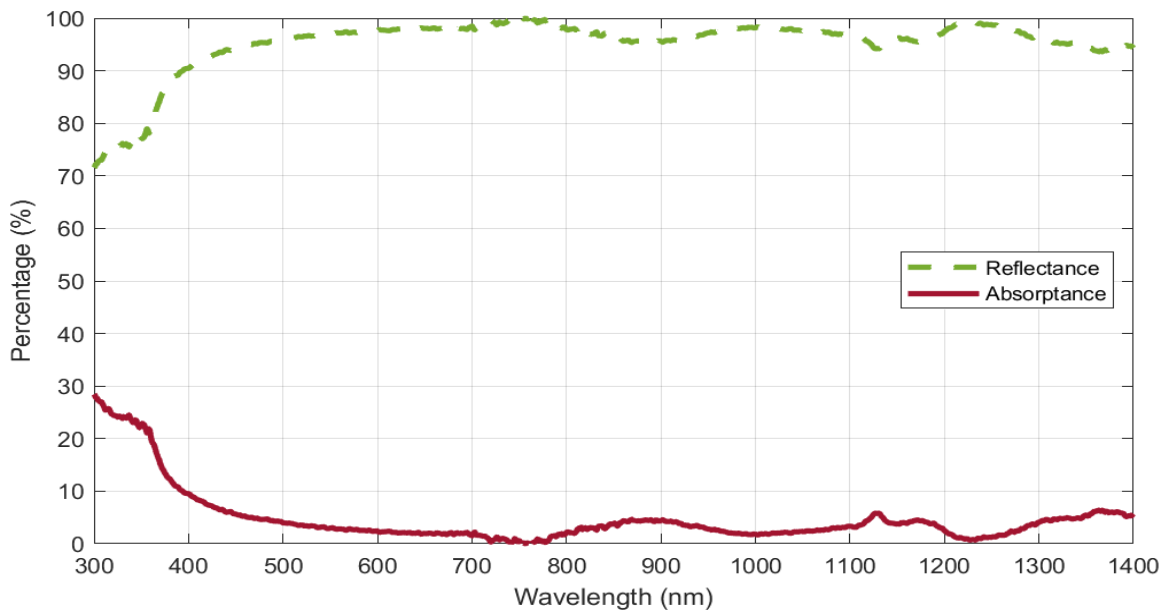


Figure 6. Spectral optical properties of the plain membrane fabricated via phase inversion

Contrasting with these results, the doped membrane (C-Cu_0.8_Y_250) exhibits a substantial increase in absorptance and thus a reduction in reflectance. Specifically, the weighted spectral reflectance and absorptance are 14.6 percent and 83.1 percent, respectively. Figure 7 exhibits the optical characterization of the doped membrane. Moreover, the stable results prove the uniform dispersion of Cu carbon coated NPs across the membrane structure and support the synthesis process previously developed.

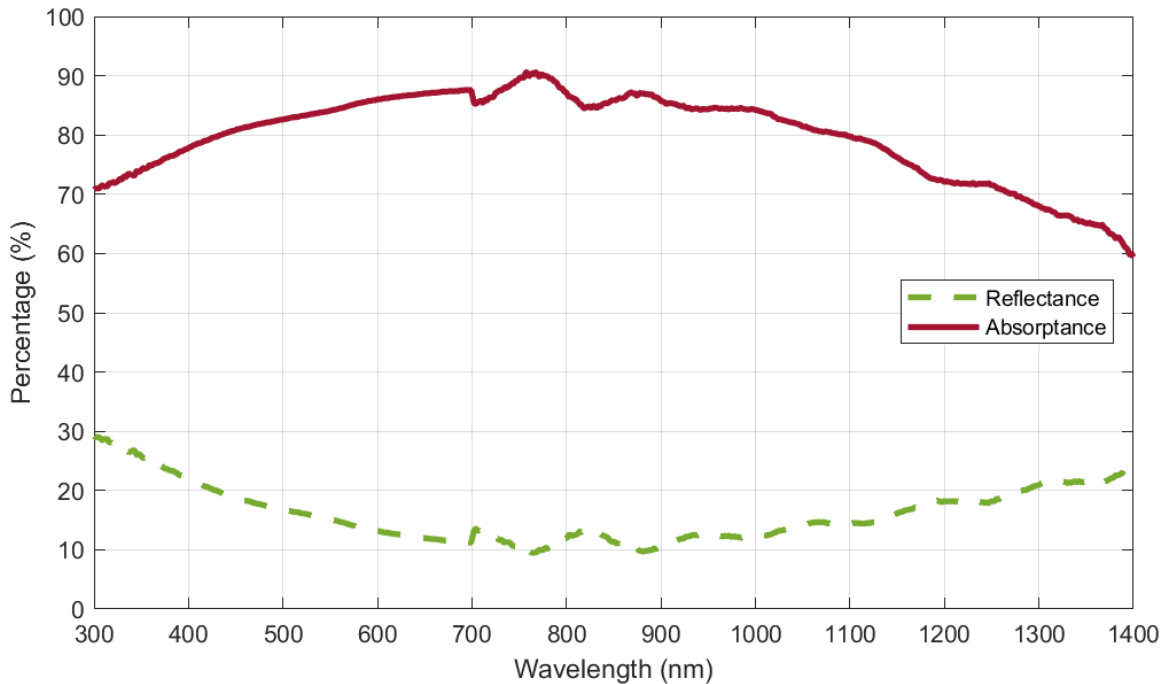


Figure 7. Spectral optical properties of the doped membrane (0.8 percent by weight copper nanopowder carbon coated) fabricated via phase inversion

2.4. Morphological Characterization

The membrane morphological structure is characterized by examining the top and bottom surfaces, the cross-sectional structure, the pore dispersion, and the dimensions. A Field Emission Scanning Electron Microscopy (FESEM; FEI Teneo) is used to obtain images of the membrane surfaces as well as of the cross-section at a micro-scale. The membrane is immersed in a liquid nitrogen bath for a few minutes, and then it is removed and shattered into small pieces for samples with clean-cut edges. A sample is glued to a stub by carbon tape and placed in a sputtering system. The sample is sputter coated with a thin layer of chromium prior to imaging for higher quality results. After the preparation of the sample, the stub is placed in the SEM chamber.

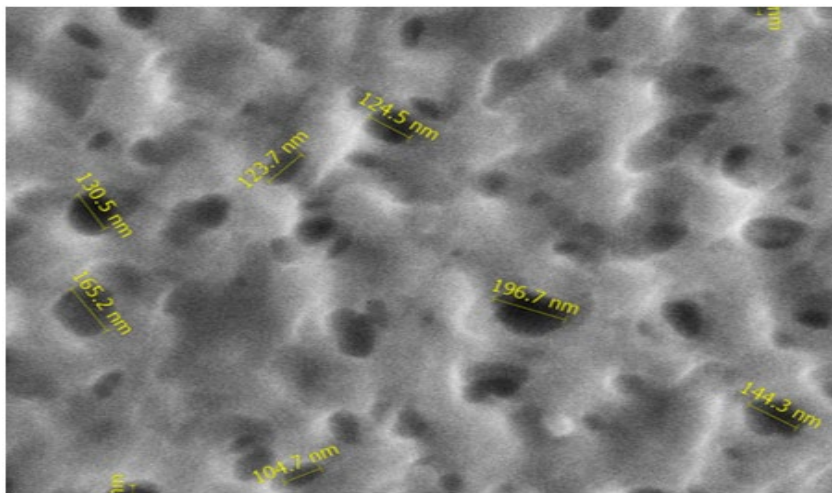
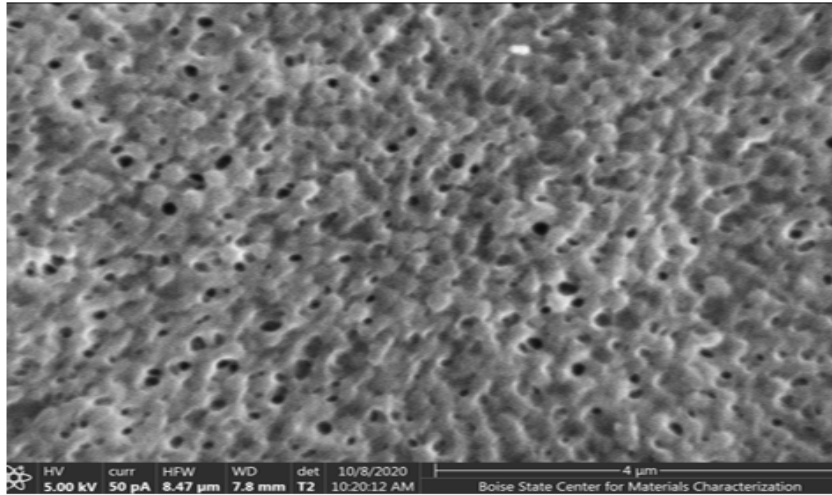
The membrane hydrophobicity is characterized by examining the contact angle (CA). A goniometer (Ramé-hart Model 90) equipped with imaging software (DROPIimage CA) measures the angle between the membrane surface and a drop of DI water by the sessile drop method. First, the goniometer is calibrated according to the manufacturer specifications. Next, the

membrane is positioned flat over the specimen stage, and the microsyringe carefully deposits a DI water drop on top of the membrane. The software measures the contact angles between the membrane surface and both sides of the drop. The mean value of both angles, automatically calculated by the software, is the actual CA value. Twelve measurements from two different locations are averaged for consistency and reported as the CA in the following sections.

Three membranes are considered for this morphological characterization. Both final plain (Plain_0.0_Y_250) and doped (C-Cu_0.8_Y_250) membranes fabricated following the custom developed synthesis process are compared to a purchased commercial membrane. The commercial membrane selected for comparison is a PVDF membrane (Millipore GVHP00010), which does not contain NPs

The morphology and cross-section of the plain and doped membranes are displayed in the following images. The top and bottom surfaces exhibit the pore dispersion and dimensions, while the cross-section exhibits the structure, thickness, and bonding to the non-woven support. Figure 8 displays the top and cross section of the plain membrane; Figure 9 displays the top and cross section of the doped membrane; and Figure 10 displays the top surface and cross section of the commercial membrane.

a) Top Surface



b) Cross-section

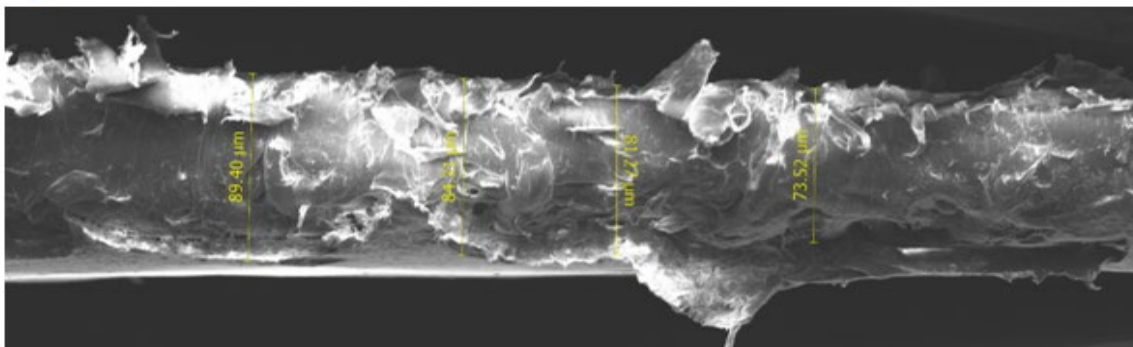
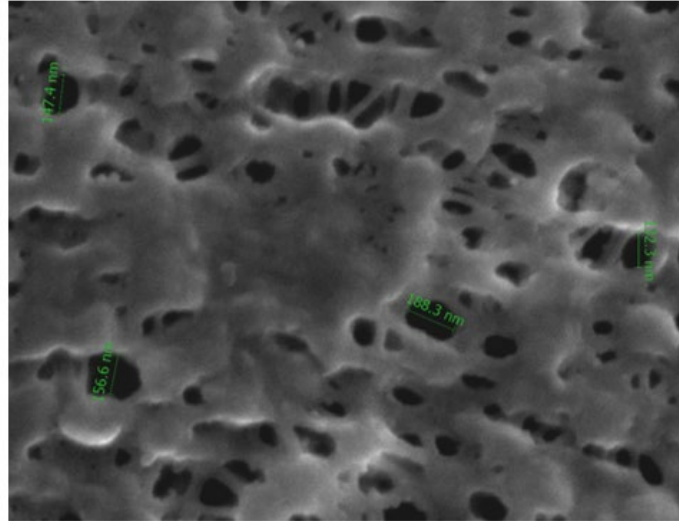
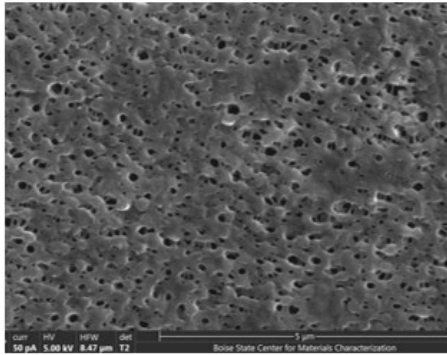


Figure 8. SEM images of the plain membrane fabricated via phase inversion: a) top surface; b) cross-section

a) Top Surface



b) Cross-section

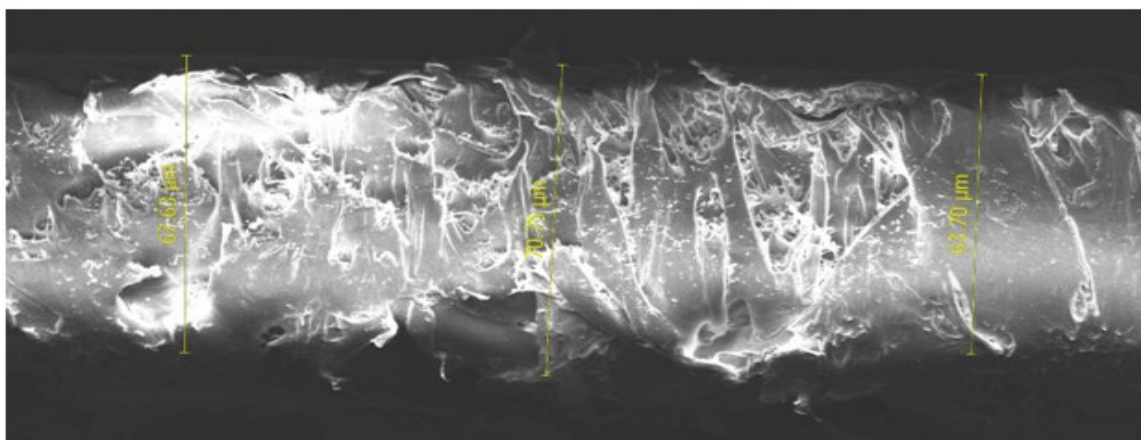
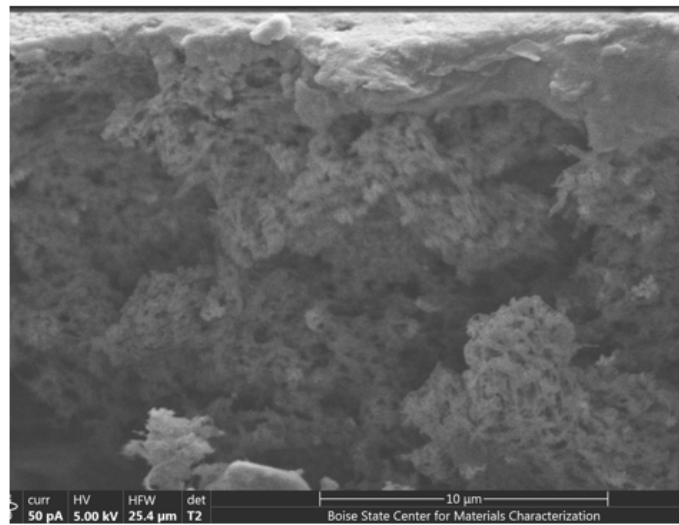
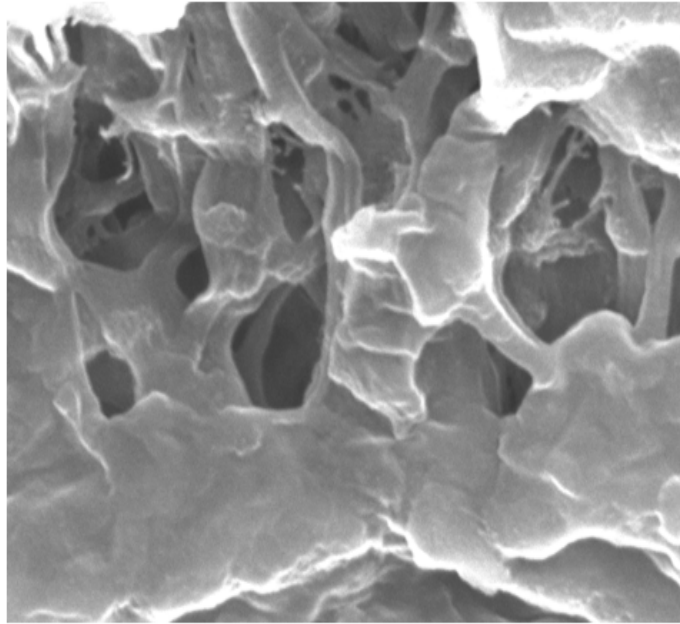
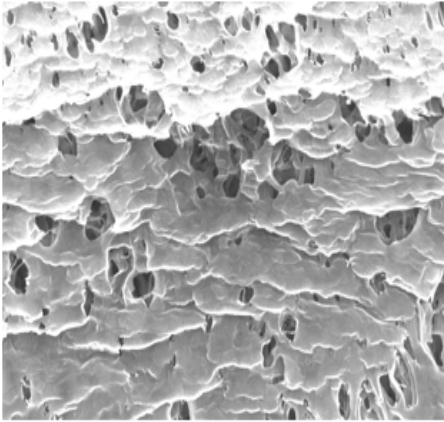


Figure 9. SEM images of the doped membrane fabricated via phase inversion: a) top surface; b) cross-section

a) Top Surface



b) Cross-section

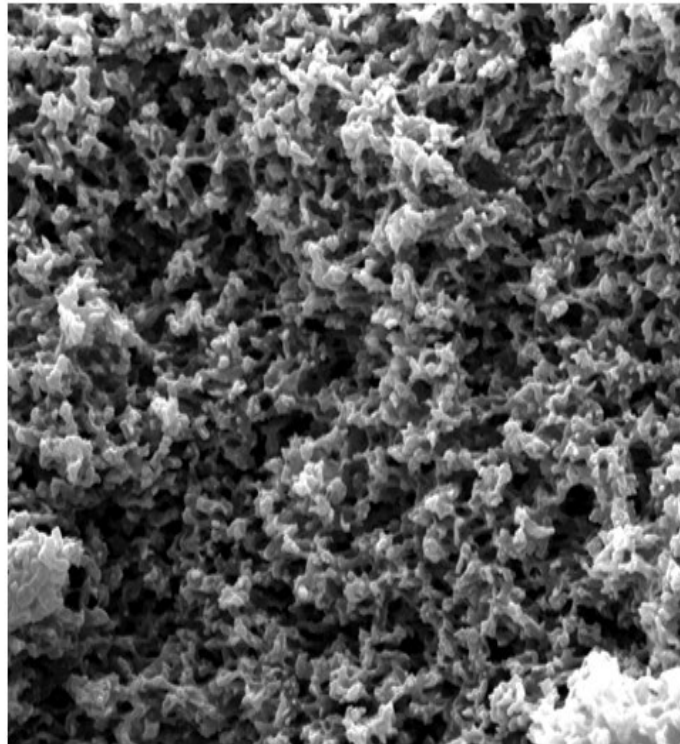
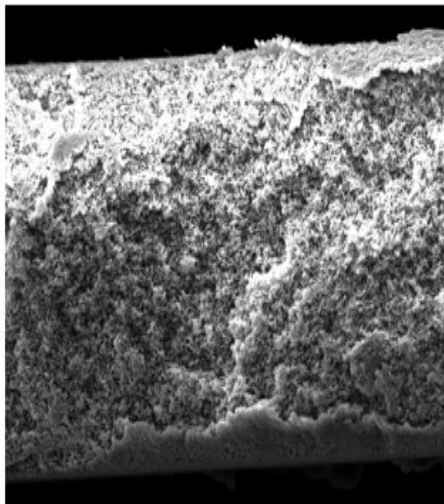


Figure 10. SEM images of a commercial PVDF membrane: a) top surface; b) cross-section

The plain and doped membranes exhibit a microporous structure with a consistent pore distribution along the surface and a pore size diameter range of 100 to 200nm, which qualify under the MD category. The microporous structure also proves the high miscibility between the polymer and the solvent (Lalia et. al., 2013). Moreover, the pores exhibit an elliptical shape rather than circular, which results in a lower tortuosity and therefore, a lower permeate flux. Although a clean-cut edge of the membranes was not always obtained due to fracture resistance, the cross sections exhibit an approximate membrane final thickness between 60 and 80 μm . In the case of the doped membrane, the structure and bonding to the support are observed. A sponge-like structure is displayed on top of the NWS fibers, confirming the hydrophobic nature of the membrane surface (Lalia et. al., 2013). Similarly, the structure of a commercial membrane in Figure 10 exhibits sponge-like structures lacking macrovoids for a hydrophobic surface. The absence of visible particles in the doped membrane images demonstrates proper mixing and uniform dispersion. Therefore, ultrasonication is a successful technique to incorporate NPs into the membrane solution.

The CA measurements obtained for all three membranes are summarized in Figure 11. The results exhibit a value of just over 100 degrees for both custom-made membranes, proving their hydrophobicity and capability for membrane distillation applications. The small load of NPs added to the doped membrane does not manifest an evident effect on its hydrophobicity as both values are similar. Moreover, their equivalent CA would theoretically translate to a similar desalination performance under no influence of any type of irradiance. However, this statement will be verified during the experimental section of the next chapter. In addition, these results are analogous to the commercial membrane, used in industrial applications, which provides more evidence of the success of the synthesis process developed.

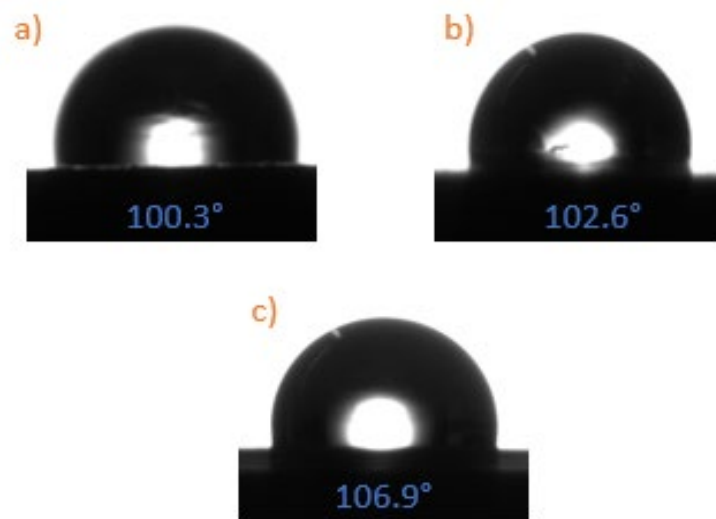


Figure 11. Membrane contact angle images and measurements: a) plain membrane; b) doped membrane; c) commercial membrane

This page intentionally left blank.

3. Hybrid System Modeling

3.1. Heat and Mass transfer Model

The model built for this study predicts both water output and electrical energy output including cell and membrane optical properties. In DCMD, the water flux can be calculated as a function of vapor pressure, water temperature, salinity, and the membrane distillation coefficient using the equation found from Gustafson et al. (Gustafson et al. 2016):

$$J_w = C_m * [P_v(T_{fm}, S_{fm}) - P_v(T_{dm}, S_{dm})] \quad (1)$$

where J_w is the water flux across the membrane, P_v the water vapor pressure, T the solution temperature, S the salinity of the water, and C_m the membrane distillation coefficient. The subscripts fm and dm refer to the properties of the feed and distillate membrane surfaces, respectively. Assuming a steady-state behavior, the heat transfer between the feed, membrane, and distillate are equal and shown by:

$$q_f = q_m = q_d \quad (2)$$

where q_f is the convective heat flux across the feed side, q_d the convective heat flux across the distillate side, and q_m the heat flux across the membrane. By introducing solar properties to the model, the convective heat flux across the feed will be affected by the waste flux from the PV cell and by the solar flux from the membrane. The solar weighted transmittance and absorbance of the PV cell are given by (Duffie and Beckman 2013):

$$\tau_{solar} = \frac{\int_0^{\infty} \tau_{\lambda} E_{\lambda} d\lambda}{\int_0^{\infty} E_{\lambda} d\lambda} \quad (3)$$

$$\alpha_{solar} = 1 - \tau_{solar} \quad (4)$$

where τ_{solar} is the solar weighted transmittance, α_{solar} is the solar weighted absorbance, τ_{λ} is the spectral transmittance, and E_{λ} is the spectral solar irradiance. The solar spectra can be found from ASTM – G173. After integrating for the solar properties, the heat flux wasted by the PV cell and the solar flux from the membrane are given by:

$$q_{PV,w} = \alpha_{solar} (1 - \eta_{PV}) E_{solar} \quad (5)$$

$$q_{solar,m} = \alpha_m \tau_{PV,solar} E_{solar} \quad (6)$$

where $q_{PV,w}$ is the waste heat flux from PV cell, $q_{solar,m}$ is the absorbed solar energy at the membrane, η_{PV} is the PV cell efficiency, E_{solar} is the total solar flux, and α_m is the solar weighted

absorbance of membrane. The heat flux at the membrane can be found from (Gustafson et al. 2016):

$$q_d = h_d(T_d - T_m) \quad (7)$$

$$q_f = h_f(T_f - T_m) + q_{PV,w} + q_{solar,m} \quad (8)$$

$$q_m = (h_v + h_c)(T_{fm} - T_{dm}) \quad (9)$$

where h_d is the distillate convective heat transfer coefficient, h_f the feed convective heat transfer coefficient, and h_v the latent heat of vaporization. Thermophysical properties of seawater functions (Nayar et al. 2016) are used to define the individual properties of the water. The model assumes that spacers are used to induce turbulent flow, which has been shown in the work done by Martínez-Díez and Vázquez-González (Martínez-Díez and Vázquez-González 2000).

The effect on the solar transmittance can be seen by comparing various types of solar cells. Two available commercial cells are a Low-E solar cell from Onyx Solar (architectural window glass) and a Dye Sensitized Solar Cell (DSSC) from Brite Solar Technologies (entering the market as glass for a greenhouse). The transmittance through these two cells can be seen in Figure 12. Two other types of solar cells that are compared in Figure 12 are a silicon bifacial cell (PVG, Earth-ON190) and a perovskite cell. As can be seen in Figure 12, the perovskite solar cell has a significantly higher transmittance than the other cells. The transmittance through the bifacial silicon cell, Onyx Solar's cell, and Brite's cell maintain values above 30 percent across large portions of the spectrum but never achieve a large level of transmittance. Figure 12 gives the solar weighted transmittance and absorbance (as defined in equations 3 and 4) as well as the solar efficiency for each cell type. Table 4 demonstrates that the best solar weighted transmittance is provided by the Onyx cell but this cell has a very low PV.

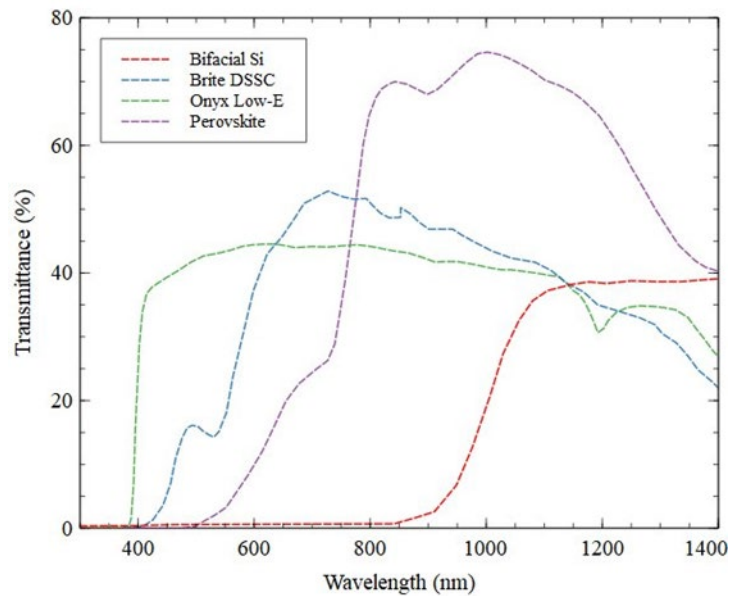


Figure 12. Transmittance of various solar cells

Table 4. Comparison of solar properties and efficiency for each solar cell used in model

Cell Type	Solar Weighted Transmittance (%)	Solar Weighted Absorptance (%)	PV Cell Efficiency (%)
Bifacial Silicon	7.79	92.2	19.4
Brite DSSC	35.3	64.7	2.5
Onyx Solar	41.6	58.4	2.8
Perovskite	34.2	65.8	14.4

3.2. Key Model Results

For this study, the feed inlet temperature is 35°C and the distillate inlet temperature is 20°C, a standard starting point for many studies, run in a counter-current flow. A key parameter for the performance of the proposed device is the concentration of the solar flux. By adding concentrators to the desalination system, the process can produce higher flux values (both electrical and water) but may affect other issues of the system. Figure 13 shows the impact of membrane length on water flux between solar fluxes of 900 W/m², 4500 W/m², and 9000 W/m² when using a perovskite PV cell. The length dependence is due to the variation in temperature.

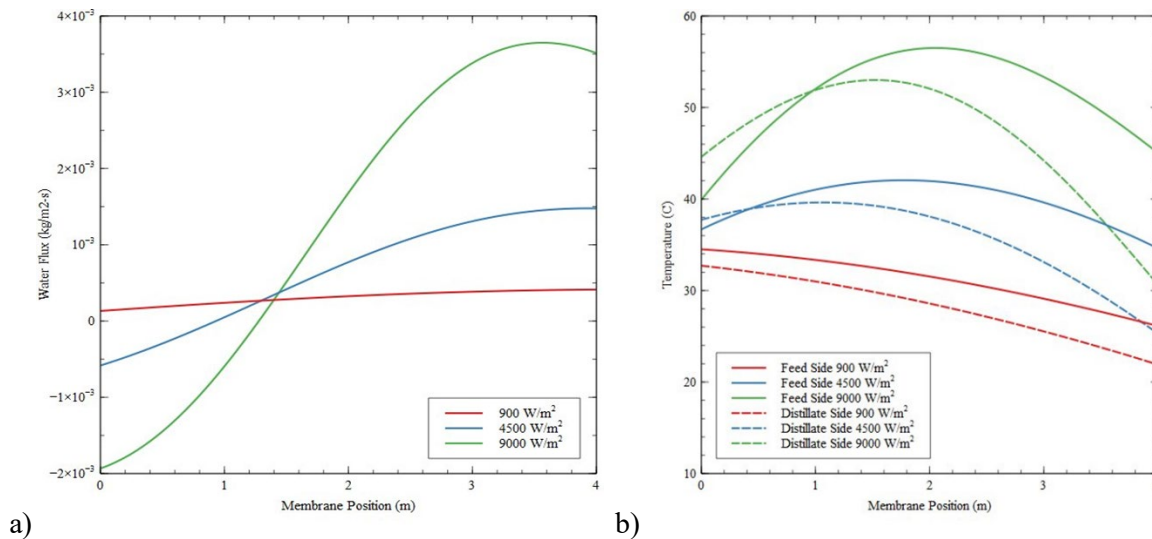


Figure 13. Water flux (a) and temperature (b) as a function of membrane position using perovskite cell

Figure 13 shows the temperature profiles for the bulk feed and membrane when using different concentrations of solar flux. At higher solar fluxes, temperature reversals can occur. These temperature differences are what cause variations in the water flux.

Another interesting result is the role of the PV cell. Figure 14 compares the differing water production as function of length and solar cell type. As can be seen, the maximum water production occurs with the Onyx and Brite cells, followed by the perovskite and bifacial cells. It should be noted that the perovskite and bifacial cells will have the highest electrical output. The water flux result isn't entirely intuitive but, upon further inspection, we discovered that the highest water production directly correlates with the product of the solar weighted cell transmittance, the solar weighted cell absorbance, and one minus the cell efficiency.

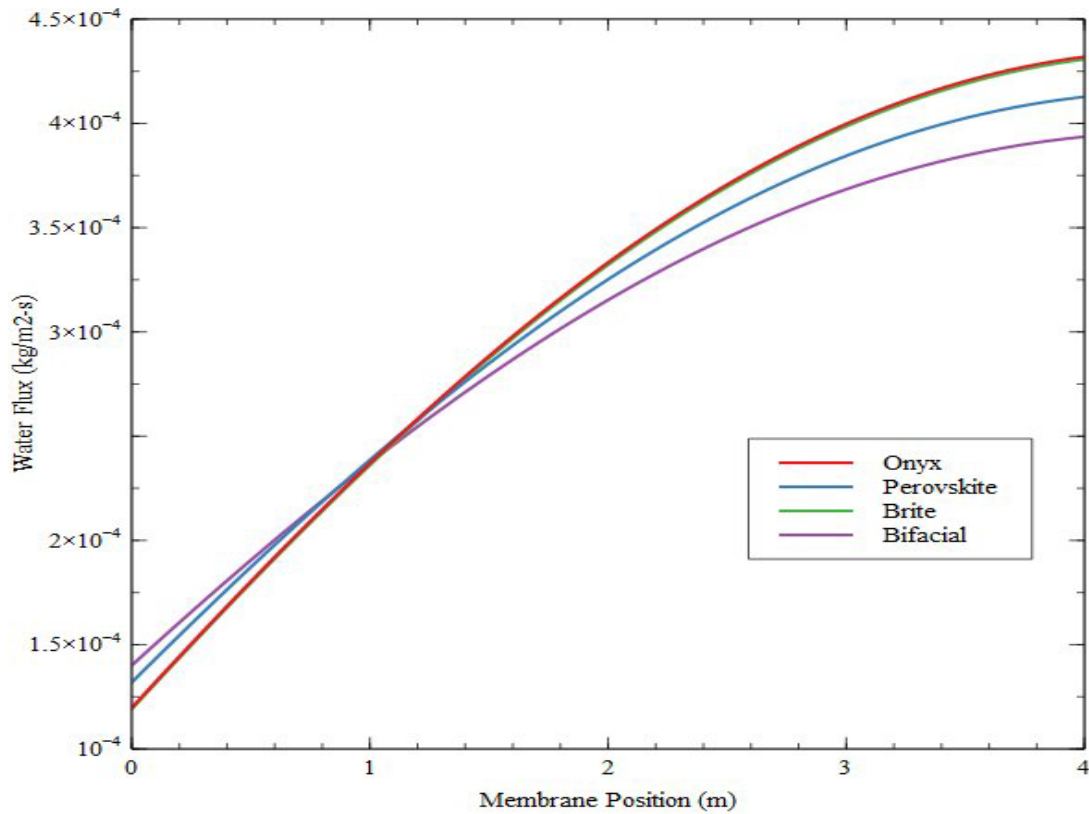


Figure 14. Water flux as a function of membrane length for different PV cells

4. Hybrid PV + Membrane Distillation

4.1. DCMD Setup

The hybrid system design consists of a custom lab-scale DCMD configuration with the proposed PV-membrane module at the core of the system. The system includes two closed loops, the feed and the permeate, that will provide the required experimental conditions and a data acquisition system to log the data. Figure 15 exhibits a scheme of the system design and a picture of the system. The feed loop, or hot loop, consists of thermocouples (Omega TC-T-NPT-G-72) and pressure transmitters (Wika A-10) in the inlet and the outlet of the membrane module, a peristaltic pump (Masterflex L/S precision pump HV-77916-10), a heater (Intelligent heater QDWS1.0), and a water tank. The water running through this closed loop is a mixture of deionized (DI) water and salt (NaCl, BioXtra, $\geq 99.5\%$ from Sigma Aldrich). The permeate loop, or cold loop, consists of the same thermocouples, pressure transmitters, water tank, and peristaltic pump. However, a cooling bath (Arctic A10 refrigerated circulator 1525108) replaces the heater, and a conductivity meter (HM Digital PSC-64D) and an electronic balance (UWE OAC-12) are included. The water running through this loop is DI water, through which the salt concentration is determined by measuring its electrical conductivity.

The data acquisition system consists of a chassis (NI cDAQ-9174) populated with a current module (NI-9203) and a temperature module (NI-9213), connected to a laptop to log the data using LabView software. The temperature module logs the temperature at the inlet and at the outlet of both loops. In contrast, the current module logs the pressure at the inlet and at the outlet of both loops and the electrical conductivity of the water in the permeate loop.

The same plain commercial PVDF membrane, used previously for a morphological comparison, is used to verify the functionality of the design. Moreover, both membranes, plain and doped, which were fabricated through the custom developed phase inversion process, are used in this study for performance characterization at indoor and outdoor conditions.

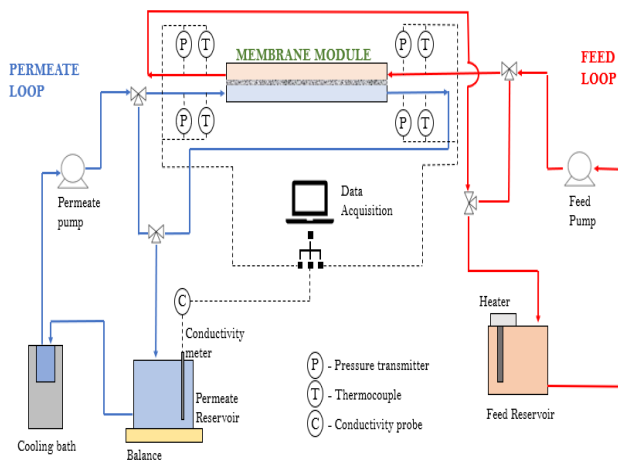


Figure 15. Schematic diagram of proposed experiment (left) and setup during outdoor on-sun testing (right)

An extensive number of experimental tests at different conditions is required to evaluate the performance of the hybrid design, including the plain and doped membranes and the PV cell on top of the membrane module. Tests at indoor conditions, with no solar irradiance, are used to determine the performance of both membranes, and tests at outdoor conditions are used to demonstrate the photothermal heating effect. This approach measures the repercussion of each design component.

A specific set of experimental conditions, defined as the standard testing conditions, is used to directly compare the membrane performance. These conditions consist of the feed loop set at a temperature of 60°C, a flow rate of 900 mL/min, and a concentration of 10 parts per thousand (ppt); the permeate loop is set at a temperature of 10°C, a flow rate of 450 mL/min, and a concentration of 0 ppt. Moreover, the membrane performance is determined by varying one parameter while maintaining the remaining parameters at their standard values.

The characterization process is applied to both plain and doped membranes and includes a range of common MD operating conditions. The feed loop covers temperatures of 50 to 80°C at 10°C intervals, flow rates of 450 to 900 mL/min (200 to 400 rpm) at intervals of 225 mL/min, and concentrations of 0 to 50 ppt at 10 ppt intervals to cover fresh, moderate, and highly saline waters above the common 35 ppt salinity of oceans. The permeate loop is set at a temperature of 10°C, a flow rate of 450 mL/min, and a concentration of 0 ppt. Furthermore, each experimental test is recorded for 90 minutes and performed twice for data reliability.

The outdoor performance characterization is performed at the standard conditions for direct comparison to the indoor performance. In the case of the doped membrane, an additional test is conducted to characterize the effect of the PV cell in the membrane performance. As with the characterization process at indoor conditions, each experimental test is recorded for 90 minutes and performed twice for data reliability.

The membrane performance is evaluated by measuring the permeate flux (J) and the salt rejection (SR), which can be determined by the following equations:

$$J = \frac{\Delta m}{A * \Delta t} \quad (10)$$

$$SR = \frac{C_f - C_p}{C_f} * 100 \quad (11)$$

The first equation is based on the weight change of the permeate tank over time. Δm is the mass increase of permeate water, A is the effective membrane area (42 cm² for this study), and Δt is the sampling time. The second equation is based on the initial and final conductivity of the feed and the permeate solutions. C_f and C_p are the feed and permeate concentration, respectively.

4.2. PV Module Characterization

Three semi-transparent solar modules (CdTe thin film from SolarFirst) rated at 30, 40, and 60 percent transparency and one solar module (amorphous silicon kindly provided by Onyx Solar), rated at 30 percent transparency, were considered in this study and are displayed in Figure 16. The nomenclature to identify the solar modules is the following: “Module type_Transparency(%)_Module size (cm²).”

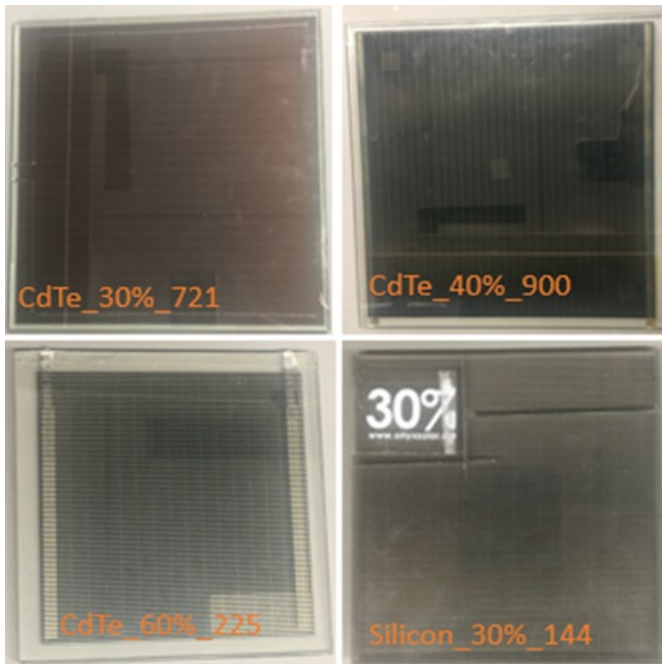


Figure 16. Semi-transparent solar modules: a) CdTe_30%_721; b) CdTe_40%_900; c) CdTe_60%_225; d) Silicon_30%_144

The solar modules are optically characterized using a miniature spectrometer (FLAME-S-XR1-ES) and a spectrophotometer (Shimadzu UV-2600) by determining their transmittance (τ). In the case of the miniature spectrometer, a spectral intensity is provided across a wavelength range of 200 to 1,000 nm. The transmittance is calculated by measuring the spectral intensity of the solar module and dividing it by a spectral intensity baseline test, without the solar module, as shown in Equation 12.

$$\tau_{\lambda} = I_{\text{cell}}/I_{\text{baseline}} \quad (12)$$

Where τ_{λ} is the spectral transmittance (%) of the solar module, I_{cell} is the spectral intensity of the solar module (counts), and I_{baseline} is the spectral intensity baseline (counts).

On the other hand, the spectrophotometer provides the spectral transmittance across a wavelength range of 300 to 1,400 nm. The wavelength range is selected to determine the amount of light in the visible spectrum, 400 to 700 nm, that the solar modules transmit to the feed stream and ultimately to the membrane. Moreover, the solar modules under analysis seem to be embedded in architectural window glass, which provides filtration of the UV and the infrared (IR) spectrums. The potential irradiance filtration from the architectural glass is determined by measuring the transmittance of the solar modules in the UV and IR spectrums. The thermal gain characterization is important since it can improve the performance by mitigating the membrane photothermal effect.

The performance and efficiency of the solar modules are measured by a solar power analyzer (Amprobe Solar 600) and a pyranometer (LI-COR LI-200R-BL-5). With a wavelength range of 400 to 1,100 nm, the pyranometer is used to measure the global horizontal solar irradiance before and during the experimental tests. It is connected to a multimeter to obtain a current output, which is then converted to an actual solar irradiance value. The measured irradiance and the solar module area are imported to the solar power analyzer. To characterize the solar module, kelvin clips probes are connected from the instrument to the solar module's poles and an auto-scan is performed. The solar power analyzer is used to determine the module performance by recording the current and voltage (I-V) curve, the maximum solar power, and the solar module efficiency, among other values.

The 60 percent semi-transparent CdTe thin film solar module (CdTe_60%_225) and the 30 percent semi-transparent silicon solar module (Silicon_30%_144) are optically characterized in Figure 17. Both solar panels, commercially available, are embedded in architectural window glass. As a result, the two solar modules have very similar optical spectrums despite having different bandgaps for the underlying solar module. Inherently, this glass limits the amount of IR light transmission into the building envelope to limit IR heating, contrary to the desired goal here. Qualitatively, this can be seen in the green tinting observed in the back-glass layer in which the PV cell is contained. Obtaining cells contained between two plates of low-iron float glass would be ideal, but these cells are not available without a custom order.

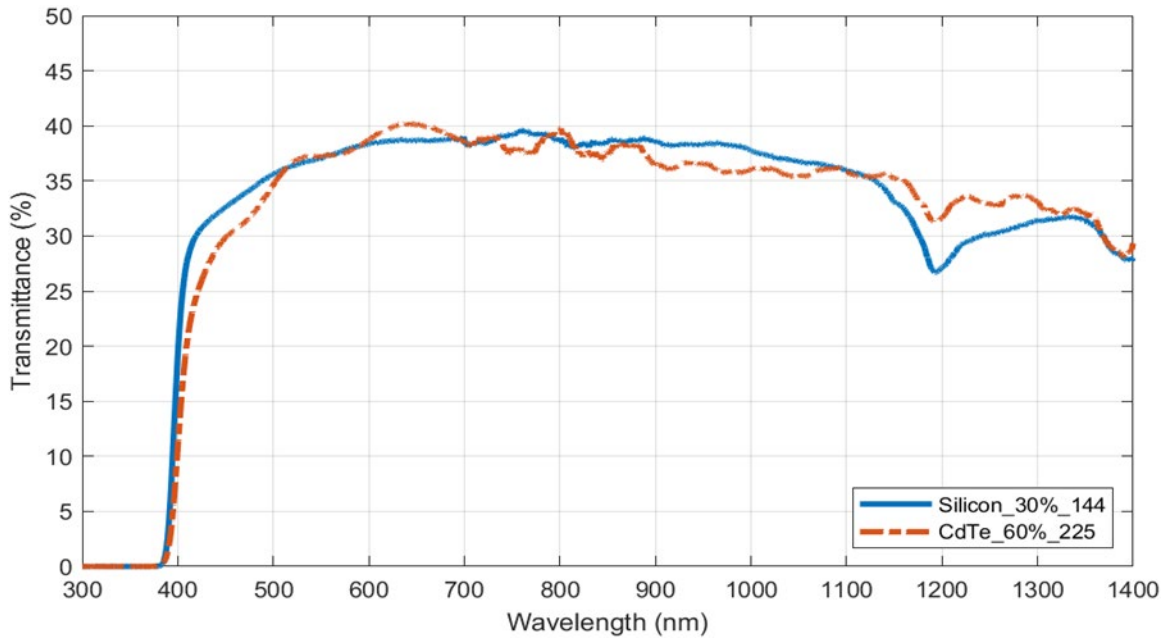


Figure 17. Spectral transmittance of two types of solar modules (CdTe_60%_225 and Silicon_30%_144) used in architectural glass applications

Table 5 also summarizes this characterization. The efficiency (η) is used for comparison due to the different dimensions of the solar modules. The CdTe_30%_721 solar module exhibits an efficiency close to 5 percent, which is well below commonly seen commercial modules but typical of semi-transparent window modules such as the ones utilized here. Furthermore, the CdTe_60%_225 module exhibits the lowest efficiency among the solar modules due to its higher transparency. The fill factor (FF), another performance indicator, is used to identify the presence of a defect or degradation of the solar module. The 60 percent transparency CdTe solar module (CdTe_60%_225) was selected to be incorporated into the hybrid membrane distillation with PV cell due to its higher transmittance. The higher transmittance results in more solar irradiance transmission through the solar module to reach the membrane and, as a result, provide a higher mitigation effect of the temperature polarization. Although this solar module exhibits a low efficiency and FF, solar modules with better performance and contained between two low-iron float glass plates can be developed.

Table 5. Summary of CdTe thin film solar panels performance characterization.

Transmittance (%T)	Vopen* (V)	Isc** (mA)	Pmax (W)	Vmax (V)	I _{max} (mA)	η (%)	FF	τ (%)
<i>CdTe_30%_721</i>	20.58	177	2.31	15.58	149	4.63	0.64	42.3
<i>CdTe_40%_900</i>	25.08	259	2.16	13.49	161	3.40	0.33	41.5
<i>CdTe_60%_225</i>	10.50	89	0.44	7.14	62	2.94	0.48	56.5

*Vopen = open-circuit voltage

**Isc = short-circuit current

5. Results and Discussion

5.1. Desalination Results Off-Sun

Figure 18 and Figure 19 exhibit the performance results of the plain (Plain_0.0_Y_250) and the commercial (C-Cu_0.8_Y_250) membranes at the standard conditions, respectively. Both membranes present a salt rejection above 99.8 percent, demonstrating their suitability for MD applications. Although they present a comparable performance, which was expected from the CA measurements, the doped membrane produces an overall higher permeate flux than the plain membrane, which can be attributed to the addition of NPs (Tijing et. al., 2016). The addition of NPs affects the membrane properties, specifically the porosity and the hydrophobicity, leading to the difference in desalination performance. The membrane porosity could be a possible reason for the permeate flux increase, but it could not be verified here. A measurement is taken every 15 minutes for a total of six measurements for each test. However, only the last four measurements of each test are averaged and reported as the permeate flux result.

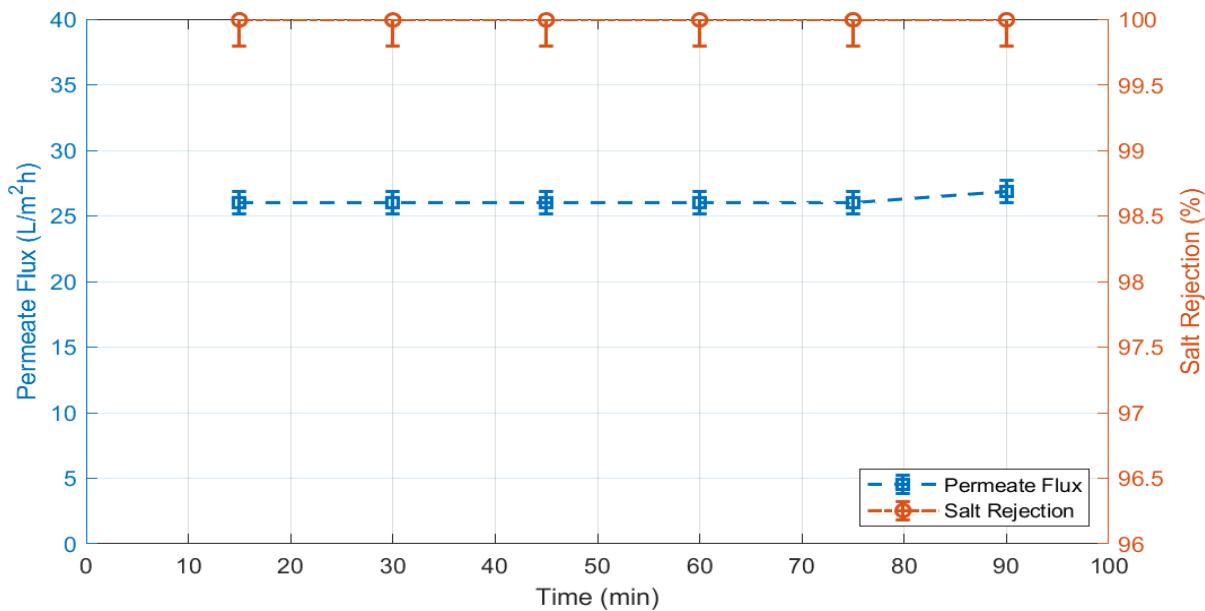


Figure 18. Plain membrane (Plain_0.0_Y_250) performance off-sun at standard conditions (permeate flux and salt rejection)

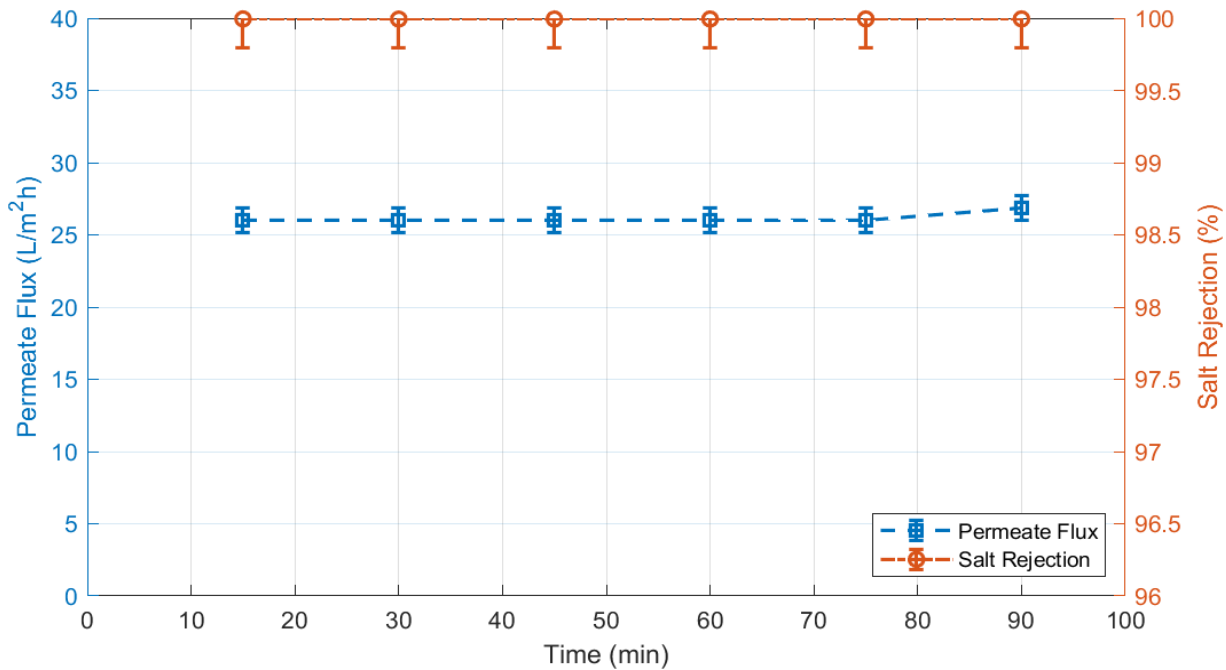


Figure 19. Doped membrane (C-Cu_{0.8}Y₂₅₀) performance off-sun at standard conditions (permeate flux and salt rejection)

Figure 20, Figure 21, and Figure 22 exhibit the mapping characterization of the plain and the doped membranes during the different experimental conditions. Two tests at each experimental condition were performed, and the average of those two tests is reported here. The overall performance of both membranes is in accordance with the results of previous studies (Cath et. al., 2004; Roshani et. al., 2018).

Figure 20 displays the performance of both membranes at different feed temperatures while the remaining parameters are maintained at standard conditions. The temperature difference between the inlet feed and the inlet permeate streams is reported instead of the feed temperatures to provide a more accurate comparison. Both membranes exhibit an increase in the permeate flux as the feed temperature increases, which is expected for a thermally-driven process. An increase in temperature results in an increase of the vapor pressure gradient between the feed and the permeate streams and thus increases the driving force. Although the permeate flux at the lower temperatures is similar for both membranes, the doped membrane seems to perform slightly better than the plain membrane at the higher temperatures, which can be attributed to the addition of NPs (Roshani et. al., 2018)). Both membranes maintained a salt rejection above 99.8 percent across all tests. In addition, the results obtained are in the range of previous studies (Cath et. al., 2004; Roshani et. al., 2018).

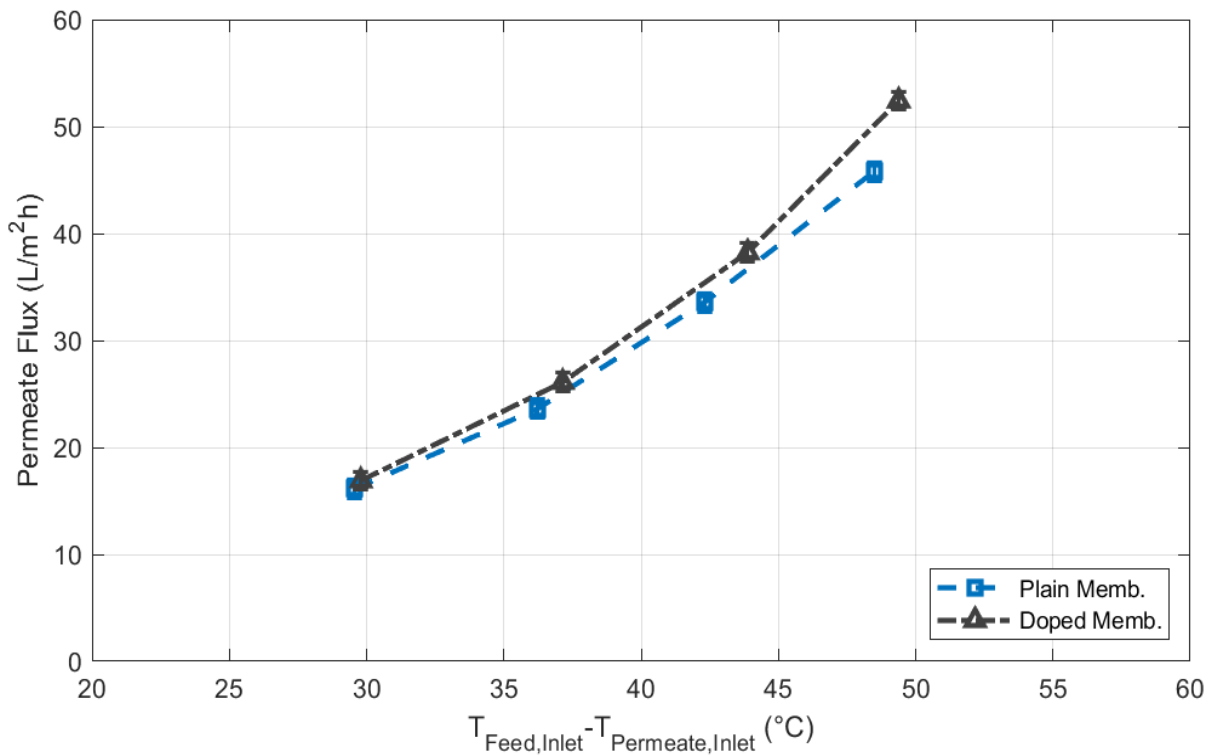


Figure 20. Plain (Plain_0.0_Y_250) and doped (C-Cu_0.8_Y_250) membrane performance off-sun at different feed temperatures (remaining experimental conditions maintained at standard conditions)

Figure 21 displays the performance of both membranes at different feed flow rates while the remaining parameters are maintained at standard conditions. As in the previous case, both membranes exhibit an increase in the permeate flux as the feed flow rate increases. An increase in the flow rate leads to an enhancement of the turbulence and mixing in the feed channel, resulting in a decrease in the thickness of the temperature boundary layer (Cath et. al., 2004). Both membranes maintained a salt rejection above 99.8 percent across all tests.

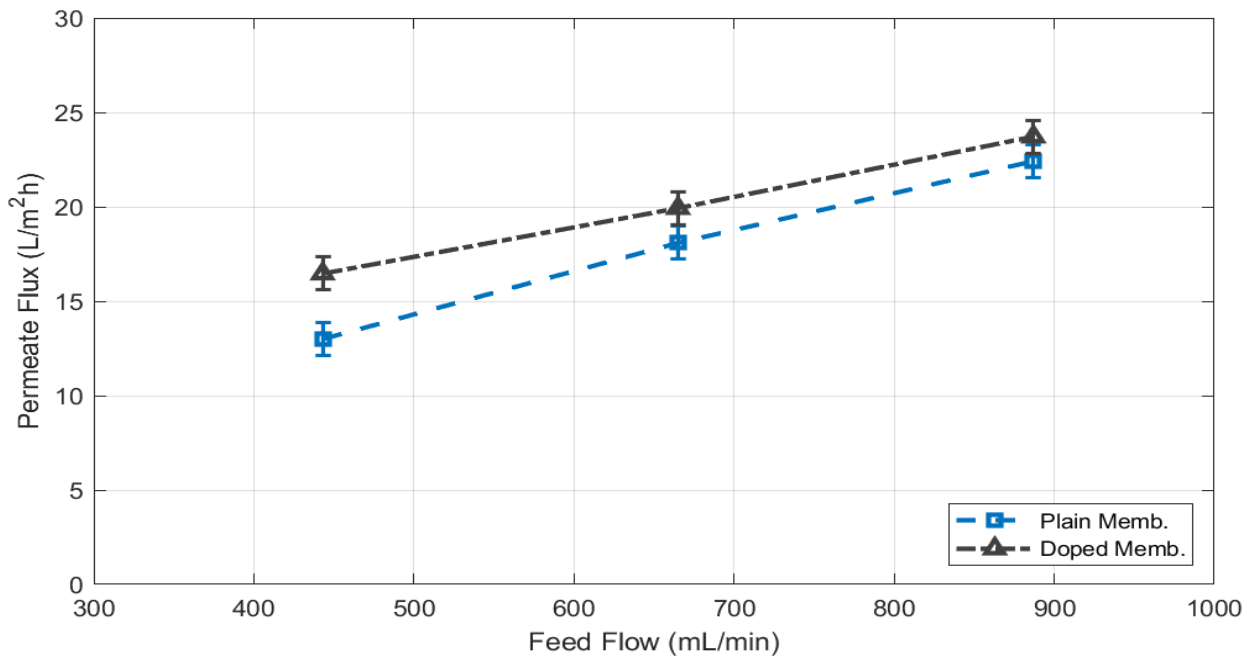


Figure 21. Plain (Plain_0.0_Y_250) and doped (C-Cu_0.8_Y_250) membrane performance off-sun at different feed flow rates (remaining experimental conditions maintained at standard conditions)

Figure 22 displays the performance of both membranes at different feed concentrations while the remaining parameters are maintained at standard conditions. In this case, both membranes exhibit a decrease in the permeate flux as the feed concentration increases. An increase in concentration leads to a reduction of the vapor pressure gradient, reducing the driving force. The contribution of the concentration polarization to the temperature boundary layer results in a reduction of the driving force for evaporation (Cath et al., 2004). Again, both membranes maintained a salt rejection above 99.8 percent across all tests.

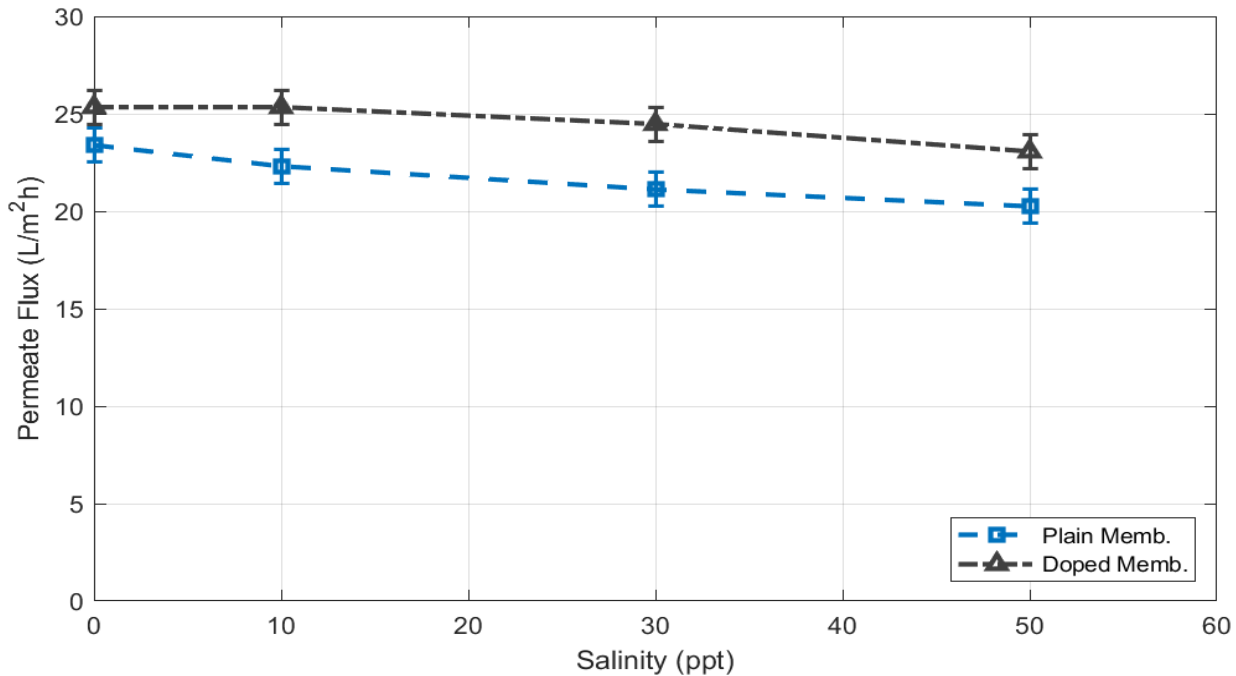


Figure 22. Plain (Plain_0.0_Y_250) and doped (C-Cu_0.8_Y_250) membrane performance off-sun at different feed concentrations (remaining experimental conditions maintained at standard conditions)

5.2. Desalination Results On-Sun

Figure 23 exhibits the photothermal effect on the plain membrane (Plain_0.0_Y_250) at standard conditions and Figure 24 summarizes the permeate performance at the same temperature difference. As with the permeate flux, the solar irradiance is averaged for the last four measurements of the test and reported as a single value. A trendline, calculated from the results at multiple temperatures in Figure 23, is included to provide another comparison indicator to the expected membrane performance at indoors conditions. In this case, an increase of 5.8 percent permeate flux was observed when exposed to a global horizontal irradiance (GHI) of 582 W/m², which can be attributed to a radiative heating effect (Dongare et. al. 2017, Politano et. al., 2016). Previous studies display a performance improvement for undoped membranes when exposed to laser radiation of concentrated intensity due to a radiative effect (Politano et. al., 2016), which in this case was observed at a smaller scale. This result was expected due to the high spectral reflectance obtained during the optical characterization of this membrane.

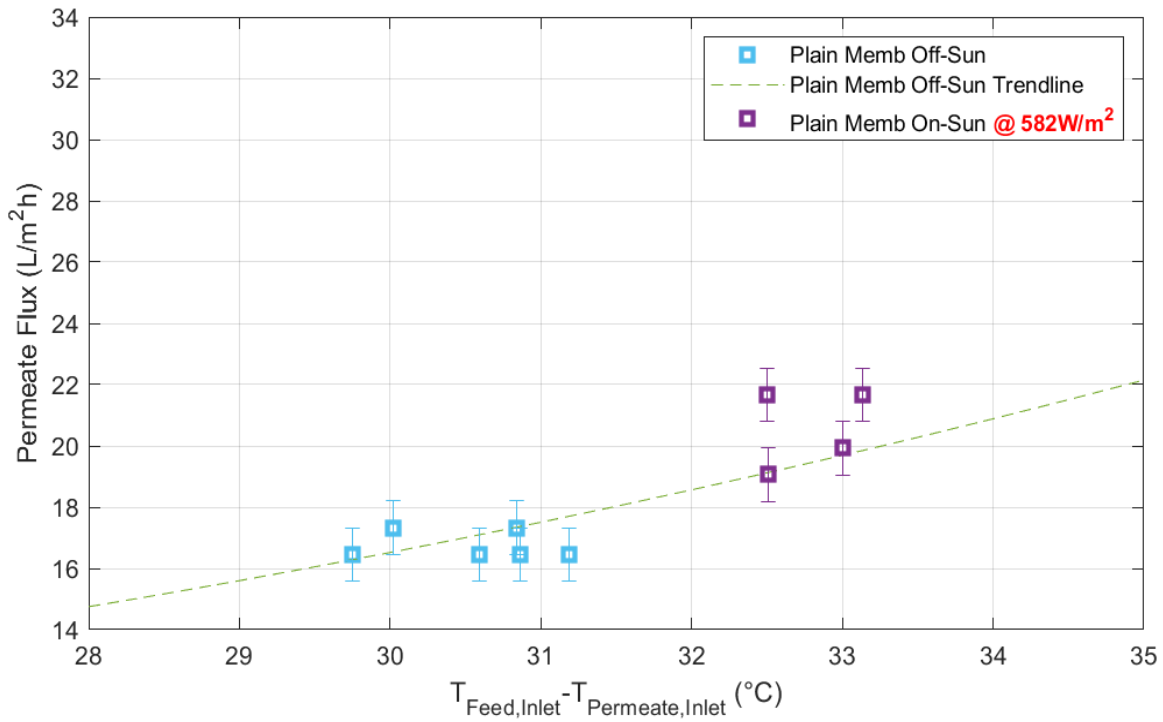


Figure 23. Photothermal effect on the plain membrane (Plain_0.0_Y_250) at standard conditions; comparison of off-sun to on-sun performances (GHI of 582 W/m²)

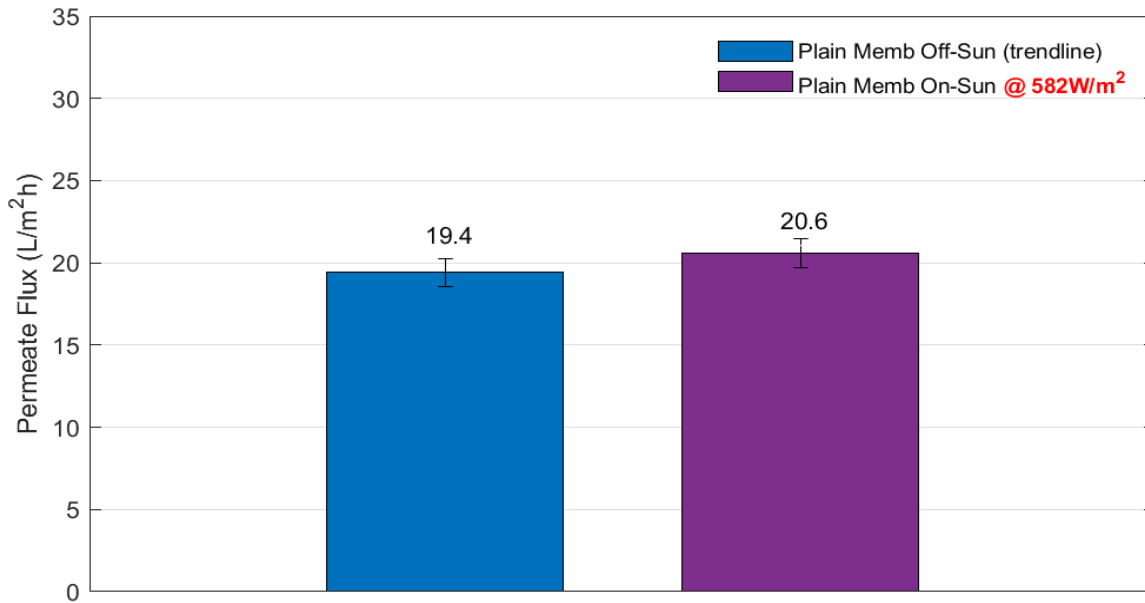


Figure 24. Summary of the photothermal effect on the plain membrane (Plain_0.0_Y_250) at standard conditions

Figure 25 and Figure 26 exhibit the photothermal effect on the doped membrane (C-Cu_0.8_Y_250) during two tests at standard conditions. The doped membrane in both cases exhibits an increase in the permeate flux when exposed to solar irradiance. Specifically, the performance improved by 15.0 percent and 32.1 percent under solar irradiance of 617 W/m² and 698 W/m², respectively. This increase in permeate flux is attributed to the radiative effect and the addition of NPs, which mitigates the temperature polarization phenomenon. The NPs act as nanoheaters inside the membrane, activated by the solar irradiance, to reduce the temperature polarization effect by increasing the membrane surface temperature (Politano et. al., 2019). The increase of the membrane surface temperature results in an increase in the vapor pressure gradient, ultimately enhancing the driving force of the process. In this case, an increase in performance was expected due to the significant increase of spectral absorption obtained during the optical characterization of this membrane.

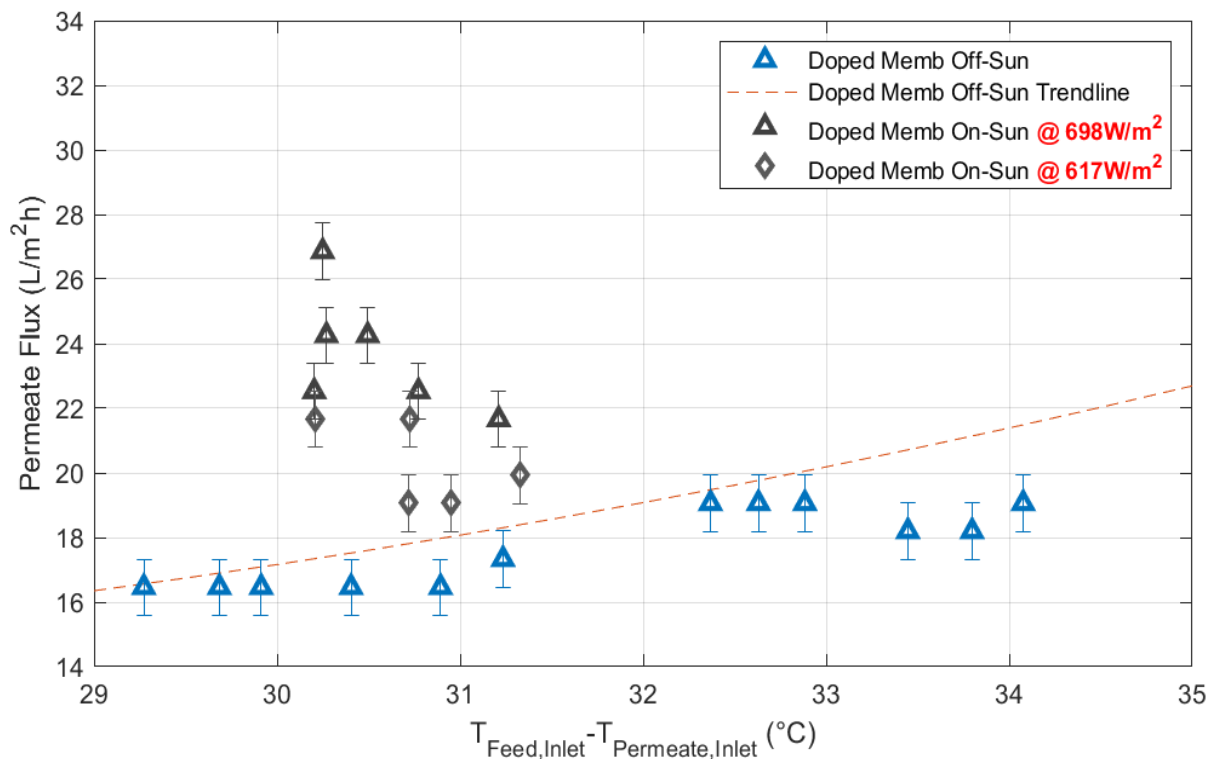


Figure 25. Photothermal effect on the doped membrane (C-Cu_0.8_Y_250) at standard conditions; comparison of off-sun to on-sun performances (GHI of 617 and 698 W/m²)

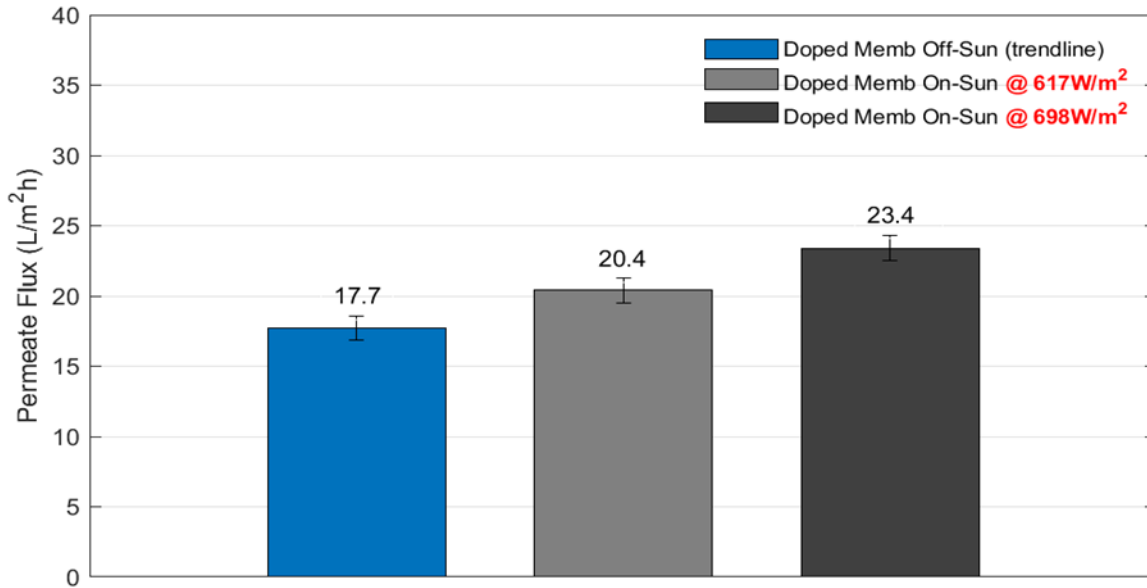


Figure 26. Summary of the photothermal effect on the doped membrane (C-Cu_0.8_Y_250) at standard conditions

As a summary, Figure 27 combines the photothermal effect on the plain and doped membranes into one graph. The performance trendlines of both membranes at indoor conditions are also included.

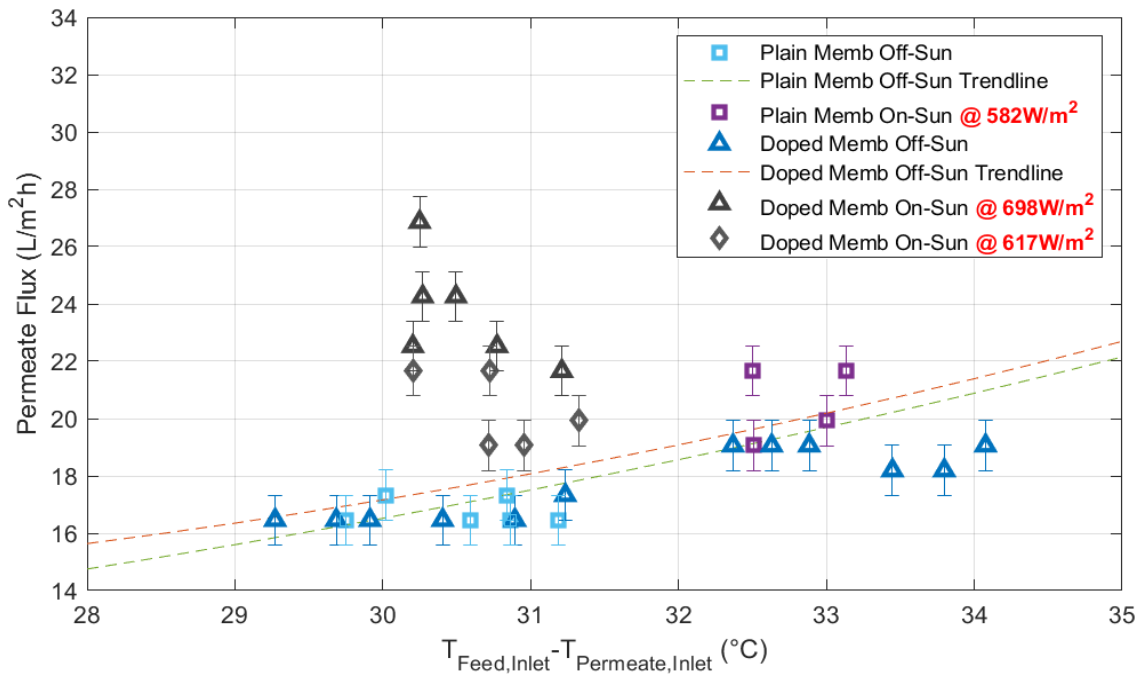


Figure 27. Summary of the photothermal effect on the plain membrane (Plain_0.0_Y_250) and the doped membrane (C-Cu_0.8_Y_250) at standard conditions

Figure 28 and Figure 29 exhibit the effect of the solar module CdTe_60%_225 on the membrane performance at standard conditions. In this case, the 60 percent transparency CdTe thin film solar module was placed on top of the membrane module and was exposed to a solar irradiance of 508 W/m². The doped membrane exhibits an increase of the permeate flux comparable to the cases with the PV cell excluded. The addition of the PV cell on top of the DCMD module was expected to reduce the solar flux to the membrane, which would result in a permeate flux drop. However, the drop in permeate flux was not observed. Adding solar modules, embedded in 7 mm thick glass, on the front side (feed) of the DCMD module reduces the heat loss to the environment, likely increasing the performance.

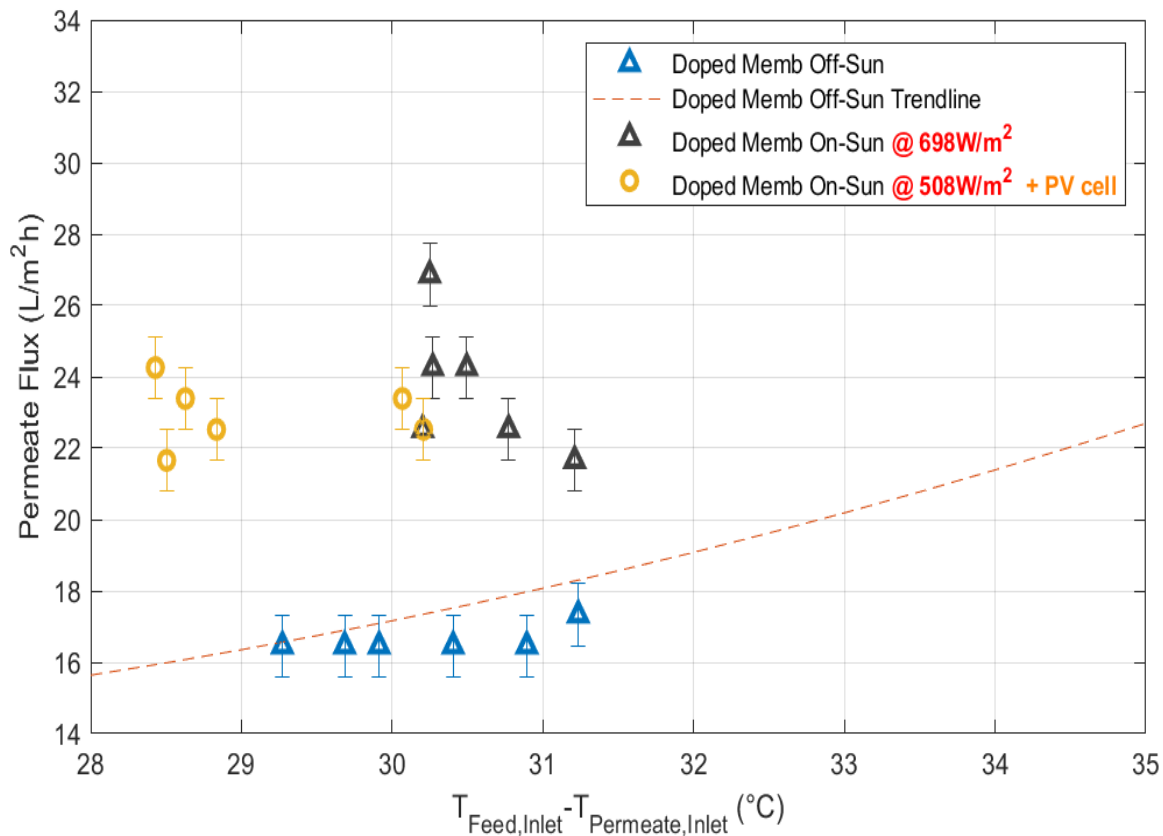


Figure 28. Solar module (CdTe_60%_225) effect on the photothermal effect of the doped membrane (C-Cu_0.8_Y_250) at standard conditions; membrane performance including and excluding the solar module (GHI of 508 and 698 W/m², respectively)

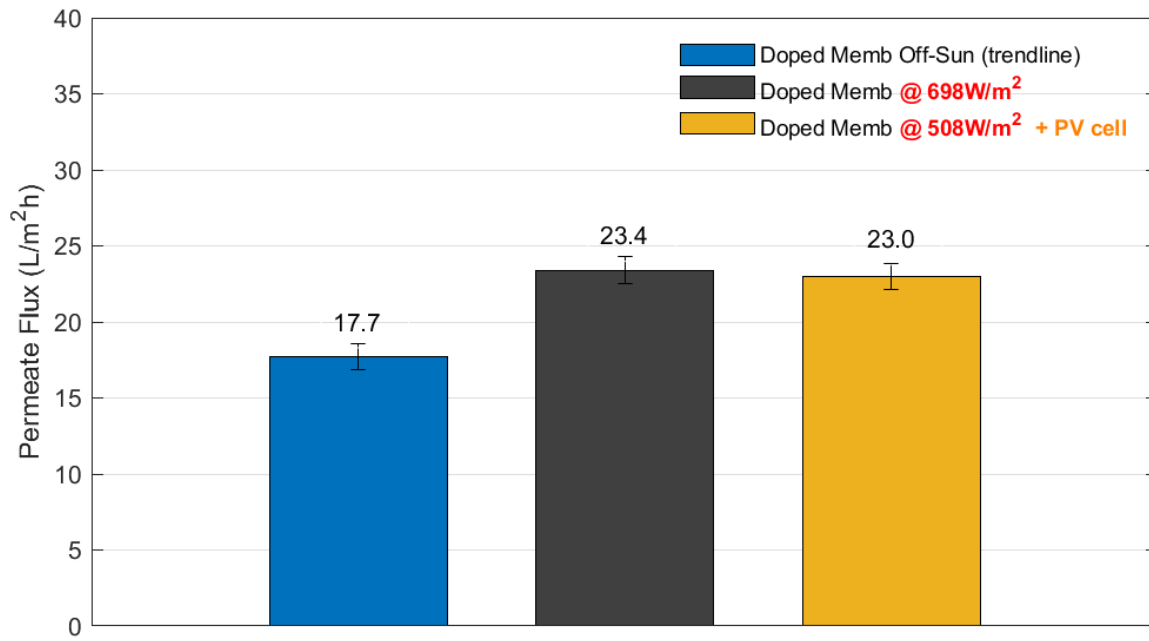


Figure 29. Summary of the solar module (CdTe_60%_225) effect on the photothermal effect of the doped membrane (C-Cu_0.8_Y_250) at standard conditions

6. Conclusions and Recommended Next Steps

6.1. Conclusions

The development of a hybrid design consisting of DCMD coupled with a PV cell has been demonstrated as a potential alternative to current desalination technologies. Membranes doped with NPs via the custom phase inversion process can be applied to MD technology to enhance the water distillation performance while maintaining the water quality. Moreover, the co-production of fresh water and electricity has been demonstrated by combining in the same design a DCMD module and a PV cell.

The development of a custom process for the fabrication of membranes has been achieved via phase inversion. The process creates membranes suitable for distillation applications such as MD with the possibility for the addition of NPs. The morphological characterization of the membranes demonstrated a microporous hydrophobic structure, and in the case of the doped membranes, uniform dispersion of NPs. The CA angle measurements above 100° proved the hydrophobic nature of the membrane, and the SEM images proved a microporous sponge-like structure with a pore size diameter range of 100 to 200 nm and a uniform dispersion of NPs. Moreover, the optical characterization of the membranes demonstrated a solar absorptance enhancement of 76.9 percent due to the addition of NPs.

The co-production of fresh water and electricity of the system has been achieved in a custom lab-scale DCMD configuration with the proposed PV-membrane module at the core of the design. The membranes demonstrated a stable and high-quality distillation for different MD operating conditions, including high saline water. Furthermore, the doped membranes proved a 15 to 32 percent distillation enhancement under solar irradiance. The NPs exposed to irradiance exhibited a photothermal heating effect capable of mitigating the main drawback of MD, the temperature polarization. Moreover, coupling a semitransparent solar module to the membrane module demonstrated little or no effect on the membrane performance, while producing useful electrical power output.

Key study results are summarized in Figure 30.

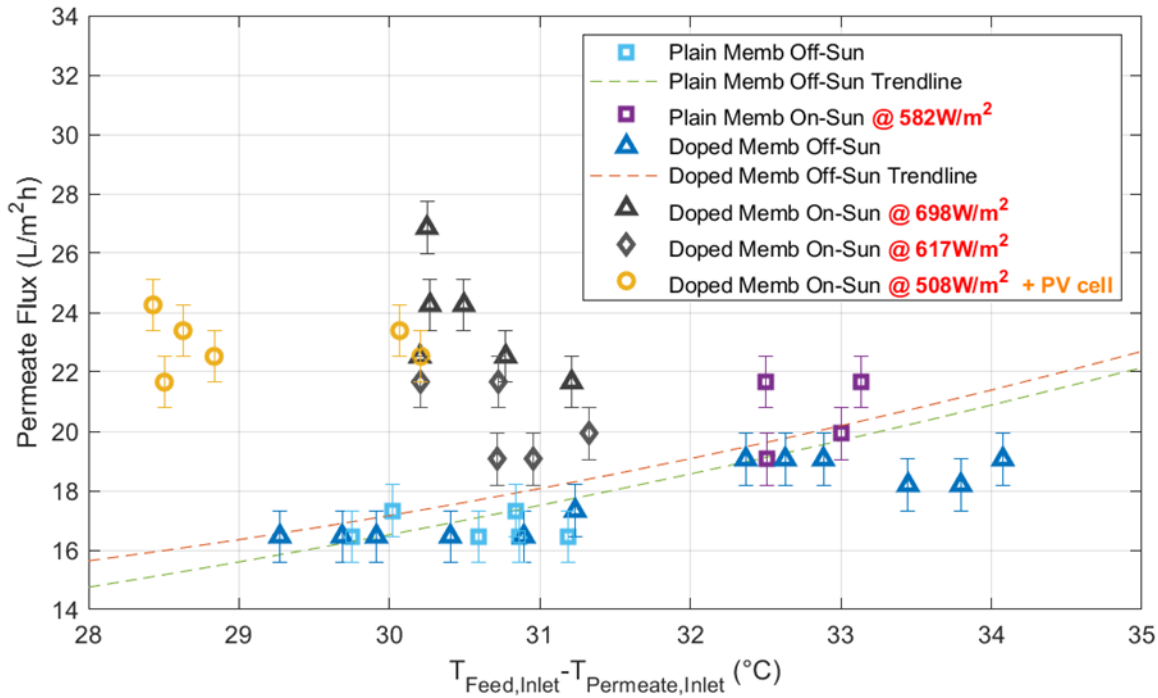


Figure 30. Desalination performance summary of the proposed hybrid PV-membrane system at standard conditions

6.2. Recommended Next Steps

Although these membranes provide distillation rates similar to the literature results, some improvements can be applied. Synthesis of unsupported membranes suitable for the large flat area needed for a hybrid PV/MD has not been achieved due to shrinkage during the phase inversion process. Continuous development work of this process should focus on the fabrication of unsupported membranes capable of incorporating NPs.

The hybrid system described in this study can also continue to be improved. The current system has been tested under irradiance less than one sun ($1,000 \text{ W/m}^2$), which presents the opportunity to combine the design with concentrated solar irradiance. Incorporating a concentrating solar energy system could continue to enhance the co-production of electricity and fresh water of the hybrid system.

Additional work can focus on developing a heat and mass transfer model capable of replicating the distillation performance of the membranes introduced in this study. That simulation model could predict the system performance and scale the design to industrial applications. Moreover, the simulation model would help identify the best combination of semitransparent solar module and membrane module for different field applications.

7. Budget Spending

The table below reports the final budget spending for the award.

Table 6. Final budget for the award

Category	Total Awarded	Total Spent through 11/30/2020	% Spent
Salaries and Wages	\$28,349.80	\$33,402.23	118%
Fringe	\$5,590.04	\$5,624.71	101%
Travel	\$3,963.00	--	0%
Supplies and Materials	\$3,869.44	\$2,836.33	73%
Graduate Tuition	\$9,646.00	\$9,475.00	98%
Indirect Costs	\$16,917.78	\$16,954.87	100%
Total	\$68,336.06	\$68,293.14	99.9%

This page intentionally left blank.

References

- Abu-Zeid, M. A. E.-R., Y. Zhang, H. Dong, L. Zhang, H.-L. Chen, and L. Hou. 2015. "A Comprehensive Review of Vacuum Membrane Distillation Technique." *Desalination* 356, pp. 1–14. <https://doi.org/10.1016/j.desal.2014.10.033>
- Al-Obaidani, S., E. Curcio, F. Macedonio, G. Di Profio, H. Al-Hinai, and E. Drioli. 2008. "Potential of Membrane Distillation in Seawater Desalination: Thermal Efficiency, Sensitivity Study and Cost Estimation." *Journal of Membrane Science* 323(1), pp. 85–98. <https://doi.org/10.1016/j.memsci.2008.06.006>
- Alkhudhiri, A., N. Darwish, and N. Hilal. 2012. "Membrane Distillation: A Comprehensive Review." *Desalination* 287(January), pp. 2–18. <https://doi.org/10.1016/j.desal.2011.08.027>
- AlMarzooqi, F. A., M. R. Bilad, and H. A. Arafat. 2016. "Development of PVDF Membranes for Membrane Distillation via Vapour Induced Crystallisation." *European Polymer Journal* 77, pp. 164–173. <https://doi.org/10.1016/j.eurpolymj.2016.01.031>
- Bilad, M. R., E. Guillen-Burrieza, M. O. Mavukkandy, F. A. Al Marzooqi, and H. A. Arafat. 2015. "Shrinkage, Defect and Membrane Distillation Performance of Composite PVDF Membranes." *Desalination* 376, pp. 62–72. <https://doi.org/10.1016/j.desal.2015.08.015>
- Blanco Gálvez, J., L. García-Rodríguez, and I. Martín-Mateos. 2009. "Seawater Desalination by an Innovative Solar-Powered Membrane Distillation System: the MEDESOL Project." *Desalination* 246(1–3), pp. 567–576. <https://doi.org/10.1016/j.desal.2008.12.005>
- Calise, F., M. Dentice d'Accadia, and A. Piacentino. 2014. "A Novel Solar Trigeneration System Integrating PVT (Photovoltaic/Thermal Collectors) and SW (Seawater) Desalination: Dynamic Simulation and Economic Assessment." *Energy* 67, pp. 129–148. <https://doi.org/10.1016/j.energy.2013.12.060>
- Cath, T. Y., V. D. Adams, and A. E. Childress. 2004. "Experimental Study of Desalination using Direct Contact Membrane Distillation: a New Approach to Flux Enhancement." *Journal of Membrane Science* 228(1), pp. 5–16. <https://doi.org/10.1016/j.memsci.2003.09.006>
- Chernyshov, M. N., G. W. Meindersma, and A. B. de Haan. 2005. "Comparison of Spacers for Temperature Polarization Reduction in Air Gap Membrane Distillation." *Desalination* 183(1–3), pp. 363–374. <https://doi.org/10.1016/j.desal.2005.04.029>
- Dobrak-Van Berlo, A., I. F. J. Vankelecom, and B. Van der Bruggen. 2011. "Parameters Determining Transport Mechanisms through Unfilled and Silicalite Filled PDMS-Based Membranes and Dense PI Membranes in Solvent Resistant Nanofiltration: Comparison with Pervaporation." *Journal of Membrane Science* 374(1–2), pp. 138–149. <https://doi.org/10.1016/j.memsci.2011.03.027>
- Dongare, P. D., A. Alabastri, S. Pedersen, K.R. Zodrow, N. J. Hogan, O. Neumann, J. Wu, T. Wang, A. Deshmukh, M. Elimelech, Q. Li, P. Nordlander, and N. J. Halas. 2017.

- "Nanophotonics-Enabled Solar Membrane Distillation for Off-Grid Water Purification." *Proceedings of the National Academy of Sciences* 114(27), pp. 6936–6941. <https://doi.org/10.1073/pnas.1701835114>
- Drioli, E., A. Ali, and F. Macedonio. 2015. "Membrane Distillation: Recent Developments and Perspectives." *Desalination* 356, pp. 56–84. <https://doi.org/10.1016/j.desal.2014.10.028>
- Duffie, J. A. and W. A. Beckman. 2013. *Solar Engineering of Thermal Processes*. <https://doi.org/10.1002/9781118671603>
- Feng, C. Y., K. C. Khulbe, T. Matsuura, and A. F. Ismail. 2013. "Recent Progresses in Polymeric Hollow Fiber Membrane Preparation, Characterization and Applications." *Separation and Purification Technology* 111, pp. 43–71. <https://doi.org/10.1016/j.seppur.2013.03.017>
- Goel, N., R. A. Taylor, and T. Otanicar. 2020. "A Review of Nanofluid-Based Direct Absorption Solar Collectors: Design Considerations and Experiments with Hybrid PV/Thermal and Direct Steam Generation Collectors." *Renewable Energy* 145, pp. 903–913. <https://doi.org/10.1016/j.renene.2019.06.097>
- Gustafson, R. D., J. R. Murphy, and A. Achilli. 2016. A Stepwise Model of Direct Contact Membrane Distillation for Application to Large-Scale Systems: Experimental Results and Model Predictions. *Desalination* 378, pp. 14–27. <https://doi.org/10.1016/j.desal.2015.09.022>
- Jain, P. K., K. S. Lee, I. H. El-Sayed, and M. El-Sayed. 2006. "Calculated Absorption and Scattering Properties of Gold Nanoparticles of Different Size, Shape, and Composition: Applications in Biological Imaging and Biomedicine." *The Journal of Physical Chemistry. B*, 110(14), pp. 7238–7248. <https://doi.org/10.1021/jp057170o>
- Khayet, M. and T. Matsuura. 2001. "Preparation and Characterization of Polyvinylidene Fluoride Membranes for Membrane Distillation." *Industrial and Engineering Chemistry Research*, 40(24), pp. 5710–5718. <https://doi.org/10.1021/ie010553y>
- Kinzer, B., K. Smith, and T. Otanicar. 2018. "Hybrid Solar Energy/Desalination Using Spectrally Selective Membrane Distillation." *International Heat Transfer Conference 16*, pp. 7643–7650. <https://doi.org/10.1615/IHTC16.nec.023330>
- Lalia, B. S., E. Guillen-Burrieza, H. A. Arafat, and R. Hashaikeh. 2013. "Fabrication and Characterization of Polyvinylidene fluoride-Co-Hexafluoropropylene (PVDF-HFP) Electrospun Membranes for Direct Contact Membrane Distillation." *Journal of Membrane Science* 428, pp. 104–115. <https://doi.org/10.1016/j.memsci.2012.10.061>
- Li, Y., T. Verbiest, R. Strobbe, and I. F. J. Vankelecom. 2014. "Silver Nanoparticles as Localized “Nano-Heaters” under LED Light Irradiation to Improve Membrane Performance." *Journal of Materials Chemistry A* 2(9), pp. 3182. <https://doi.org/10.1039/c3ta14406b>
- Li, Y., T. Verbiest, and I. Vankelecom. 2013. "Improving the Flux of PDMS Membranes via Localized Heating through Incorporation Of Gold Nanoparticles." *Journal of Membrane Science* 428, pp. 63–69. <https://doi.org/10.1016/j.memsci.2012.10.050>
- Lind, M. L. 2018. *Nanophotonic Pervaporation Desalination*. (213 pp.).

- Lounis, S. D., E. L. Runnerstrom, A. Bergerud, D. Nordlund, and D. J. Milliron. 2014. "Influence of Dopant Distribution on the Plasmonic Properties of Indium Tin Oxide Nanocrystals." *Journal of the American Chemical Society* 136, pp. 7110–7116.
- Mahdi, M., A. Shirazi, and A. Kargari. 2015. "A Review on Applications of Membrane Distillation (MD) Process for Wastewater Treatment." *Journal of Membrane Science and Research* 1, pp. 101–112.
- Manawi, Y. M., M. A. M. M. Khraishah, A. K. Fard, F. Benyahia, and S. Adham. 2014. "A Predictive Model for the Assessment of the Temperature Polarization Effect in Direct Contact Membrane Distillation Desalination of High Salinity Feed." *Desalination* 341, pp. 38–49. <https://doi.org/10.1016/j.desal.2014.02.028>
- Martínez-Díez, L. and M. I. Vázquez-González. 2000. "A Method to Evaluate Coefficients Affecting Flux in Membrane Distillation." *Journal of Membrane Science* 173(2), pp. 225–234. [https://doi.org/10.1016/S0376-7388\(00\)00362-8](https://doi.org/10.1016/S0376-7388(00)00362-8)
- Nayar, K. G., M. H. Sharqawy, L. D. Banchik, and J. H. Lienhard V. 2016. "Thermophysical properties of seawater: A review and new correlations that include pressure dependence." *Desalination* 390, pp. 1–24. <https://doi.org/10.1016/j.desal.2016.02.024>
- Oldenburg, S. J., R. D. Averitt, S. L. Westcott, and N. J. Halas. 1998. "Nanoengineering of Optical Resonances." *Journal of Communicable Diseases* 19(1), pp. 86–88.
- Politano, A, A. Cupolillo, G. Di Profio, H. A. Arafat, G. Chiarello, and E. Curcio. 2016. "When Plasmonics Meets Membrane Technology." *Journal of Physics: Condensed Matter* 28(36), p. 363003. <https://doi.org/10.1088/0953-8984/28/36/363003>
- Politano, A., G. Di Profio, E. Fontananova, V. Sanna, A. Cupolillo, and E. Curcio. 2019. "Overcoming Temperature Polarization in Membrane Distillation by Thermoplasmonic Effects Activated by Ag Nanofillers in Polymeric Membranes." *Desalination* 451, pp. 192–199. <https://doi.org/10.1016/j.desal.2018.03.006>
- Qtaishat, M. R. and F. Banat. 2013. "Desalination by Solar Powered Membrane Distillation Systems." *Desalination* 308, pp. 186–197. <https://doi.org/10.1016/j.desal.2012.01.021>
- Roshani, R., F. Ardeshiri, M. Peyravi, and M. Jahanshahi. 2018. "Highly Permeable PVDF Membrane with PS/Zno Nanocomposite Incorporated for Distillation Process." *RSC Advances* 8(42), pp. 23499–23515. <https://doi.org/10.1039/c8ra02908c>
- Summers, E. K. and V. J. H. Lienhard. 2013. "A Novel Solar-Driven Air Gap Membrane Distillation System." *Desalination and Water Treatment* 51(7–9), pp. 1344–1351. <https://doi.org/10.1080/19443994.2012.705096>
- Tijing, L. D., Y. C. Woo, W. G. Shim, T. He, J.-S. Choi, S. H. Kim, and H. K. Shon. 2016. "Superhydrophobic Nanofiber Membrane Containing Carbon Nanotubes for High-Performance Direct Contact Membrane Distillation." *Journal of Membrane Science* 502, pp. 158–170. <https://doi.org/10.1016/j.memsci.2015.12.014>
- Vanherck, K., I. Vankelecom, and T. Verbiest. 2011. "Improving Fluxes of Polyimide

Membranes Containing Gold Nanoparticles by Photothermal Heating." *Journal of Membrane Science* 373(1–2), pp. 5–13. <https://doi.org/10.1016/j.memsci.2011.02.010>

Wang, P. and T. S. Chung. 2015. "Recent Advances in Membrane Distillation Processes: Membrane Development, Configuration Design and Application Exploring." *Journal of Membrane Science* 474, pp. 39–56. <https://doi.org/10.1016/j.memsci.2014.09.016>